Robotica (2026), **44**, pp. 2284–2312
doi:10.1017/S0263574726103610

CAMBRIDGE UNIVERSITY PRESS

RESEARCH ARTICLE

Development of a structurally compact magnetorheological prosthetic knee joint with obstacle-crossing function

Lei Xu[1,2,3], Chao Wang[1,2], Qiuxia Fan[1,2], Qianqian Zhang[1,2] and Yuhui Liu[1]

[1]Precision and Vibration Control Innovation Team, Shanxi University, China
[2]Quantum Precision Measurement and Vibration Control Innovation Center, Shanxi University, China
[3]Robot Control Laboratory, Anzhengda Power Engineering Company Limited, China
Corresponding author: Qiuxia Fan; E-mail: fanqiuxia0808@126.com

Received: 8 November 2025 UTC; **Revised:** 16 April 2026 UTC; **Accepted:** 14 May 2026 UTC;
First published online: 22 September 2026 UTC

Keywords: magnetorheological; prosthetic knee joint; four-bar linkage mechanism; micro linear motor; magnetic circuit

Abstract

To address the difficulty of simultaneously achieving motion bionics, active driving capability, and structural compactness in prosthetic knee joints, a structurally compact magnetorheological prosthetic knee joint (SCMRPK) with obstacle-crossing function is proposed in this paper. The SCMRPK combines a four-bar linkage mechanism and a linear magnetorheological actuator (LMRA). By integrating a micro linear motor into the piston rod of an MR damper, the LMRA combines the active and semi-active modes, enabling it to output driving force in the active mode and controllable damping force in the semi-active mode. The four-bar linkage mechanism is used to mimic the variation of the instantaneous center of rotation of the human knee. The structure and working principle of the SCMRPK are presented. A key dimensional design method for the LMRA magnetic circuit is proposed, and simulation and experimental tests are conducted to verify the effectiveness of the designed magnetic circuit. A control method for the SCMRPK is developed, and a prototype is fabricated. Under a locking current of 1.5 A, the LMRA prototype achieves stable displacement tracking in active mode. At a walking speed of 1.2 m/s, the semi-active mode of the SCMRPK prototype yields a root mean square error of 1.54° between the measured and ideal knee angles. In active mode, the SCMRPK-based lower-limb prosthesis successfully crosses an obstacle 0.3 m high. These results demonstrate that the proposed SCMRPK is compact and capable of achieving a relatively natural gait and obstacle crossing.

1. Introduction

Due to traffic accidents, natural disasters, industrial injuries, and diseases, a large number of people worldwide suffer from lower limb amputation or lower limb dysfunction each year [1]. Loss of lower limb function leads to the loss of walking ability and seriously affects patients' daily life and independent mobility. Owing to current limitations in medical technology, lower limb function is difficult to restore naturally [2]. Therefore, lower limb prostheses, exoskeletons, and lower limb assistive robots have become important technical approaches for restoring walking ability.

Semi-active control devices based on magnetorheological fluid (MRF) have been widely applied in various lower limb assistive devices because of their fast response and continuously adjustable damping characteristics [3, 4]. In prosthetic systems for lower limb amputees, magnetorheological technology has mainly been used for damping regulation in knee and ankle joints, including low-cost prosthetic knees [5], controllable ankle–foot prostheses [6], and optimized MR dampers for prosthetic ankle joints [7–10]. In assistive exoskeletons, MR dampers and MR actuators have been used to provide adjustable joint support and damping control [11, 12]. In lower-limb robotic and rehabilitation systems, MR-based

© The Author(s), 2026. Published by Cambridge University Press.

https://doi.org/10.1017/S0263574726103610 Published online by Cambridge University Press

actuation units have also been applied to knee and ankle joint mechanisms to achieve compliant control and personalized rehabilitation assistance [13, 14]. These studies demonstrate the good application potential of magnetorheological technology in knee and ankle joints.

Among lower limb prosthetic joints, the knee joint is the most critical one because it bears high loads and performs complex motions during lower limb movement. In the structural design of magnetorheological prosthetic knee joints, the combination of a single-axis structure and an MR damper has been widely adopted [15–22]. Carlson et al. [15], Kim et al. [16], and Herr et al. [17, 18] developed MR-damper-based prosthetic knee designs for trajectory tracking and damping control. Zuo et al. [19] further proposed a robust control method to improve swing phase trajectory tracking. To satisfy the walking requirements of semi-active prosthetic knee joints, Fu et al. [20], Song et al. [21], and Saini et al. [22] optimized the structure and parameters of MR dampers. Related MR-based knee joint designs have also been extended to exoskeleton applications [23–25]. Although these studies have made progress in structural design and control methods, some limitations still remain. On the one hand, the rotational form of single-axis prosthetic knee joints is too simple to mimic the variation of the instantaneous center of rotation of the human knee. On the other hand, MR dampers are semi-active actuators and cannot provide active torque, which limits their performance in uphill walking and obstacle-crossing conditions.

In fact, flexion and extension of the human knee do not occur about a fixed axis. Instead, they are jointly formed by rolling and sliding between the femur and the tibia, and the center of rotation gradually shifts from front to rear as the flexion angle changes [26]. Existing studies have shown that four-bar linkage mechanisms can effectively mimic the variation of the instantaneous center of rotation of the human knee [27, 28]. Based on this characteristic, researchers have combined four-bar linkages with MR dampers and applied them to prosthetic knee joints [29–33]. Ochoa-Diaz et al. [29], Xie et al. [30], and Xu et al. [31] integrated MR dampers with four-bar linkages to construct magnetorheological four-bar prosthetic knee joints. Mohamed et al. [32] proposed a design method for four-bar prosthetic knee mechanisms by combining kinematic constraints and intelligent optimization algorithms, while Zhang et al. [33] improved the swing phase trajectory tracking accuracy of this type of prosthetic knee joint by introducing an iterative learning control method. Compared with single-axis structures, four-bar magnetorheological prosthetic knee joints can better mimic the variation of the instantaneous center of rotation of the human knee. However, these structures still rely on MR damping regulation and lack active driving capability.

Against this background, researchers began to introduce active actuation units such as motors into prosthetic knee joints [34–43] to supplement the active driving capability of the joint. Park et al. [35] and Andrade et al. [36] developed prosthetic systems that combined motor driving and magnetorheological damping to realize multiple operating modes. Arteaga et al. [37] designed an actively controlled knee prosthesis based on an MRF torque limiter to achieve real-time tracking of joint torque and angle. Gao et al. [38, 39] further introduced a DC motor and an MR damper into a prosthetic knee joint to improve energy utilization efficiency and motion adaptability during walking. In addition, Ma et al. [40] developed an MR actuator with energy regeneration capability for knee gait assistance, while Chen et al. [41] and Wang et al. [42] extended MR-based actuation designs to lower limb exoskeletons. These active lower limb assistive devices are shown in Figure 1, and the dimensions of their knee joint structures are listed in Table I. These studies indicate that, after the introduction of motors, magnetorheological prosthetic knee joints can achieve active joint driving and meet the demand for active driving force under conditions such as obstacle crossing.

In summary, to better mimic the natural knee, a prosthetic knee joint should simultaneously possess the instantaneous center of rotation characteristic, semi-active damping regulation capability, and active driving capability. At present, few studies have integrated these three functions into a single prosthetic knee joint. As shown in Figure 1 and Table I, most current designs combine an MR damper with a motor, but the superposition or parallel arrangement of the two leads to an excessively large overall size. Unlike exoskeletons and robotic systems, prosthetic knee joints for transfemoral amputees are subject to stricter requirements on structural size and appearance, and their overall dimensions should be controlled within the range of the natural human lower limb. Therefore, under dimensional constraints, it is necessary to

https://doi.org/10.1017/S0263574726103610 Published online by Cambridge University Press

Table I. *The dimensions of the knee joint within the various active lower limb assistive devices.*

Literature	Park [35]	Andrade [36]	Arteaga [37]	Gao [38]	Ma [40]	We
Length	80 mm	117 mm	70 mm	85 mm	92 mm	60 mm
Width	110 mm	80.5 mm	50 mm	60 mm	65 mm	53 mm

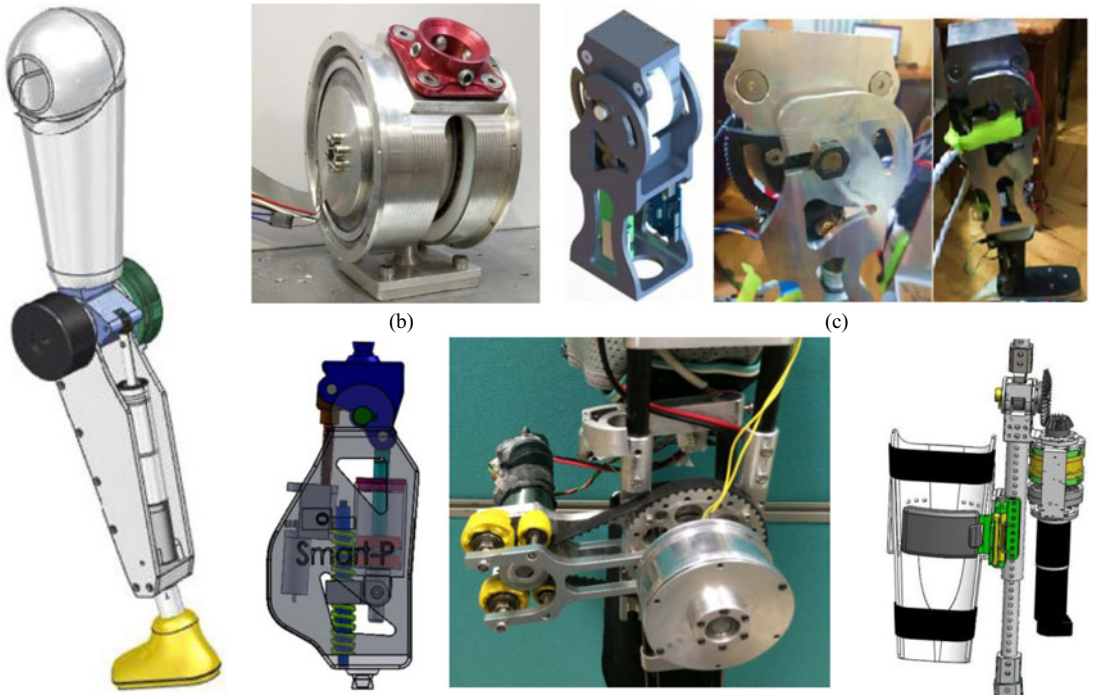


Figure 1. *The active lower limb assistive devices: (a) a prosthetic leg by Park et al. from [35]. (b) the active magnetorheological prosthetic knee by Andrade et al. from [36]. (c) the human knee smart prosthesis by Arteaga et al. from [37]. (d) the smart prosthetic knees by Gao et al. from [38]. (e) the assistive knee brace by Ma et al. from [40]. (f) the mechanical structure of MRSEA by Chen et al. from [41].*

design a prosthetic knee joint for transfemoral amputees that simultaneously possesses bionic rotational characteristics, semi-active damping regulation capability, and active driving capability.

To address the above issues, this paper designs a structurally compact magnetorheological prosthetic knee joint (SCMRPK) by combining a four-bar linkage mechanism with a linear magnetorheological actuator (LMRA). The four-bar linkage mechanism is used to mimic the variation of the instantaneous center of rotation of the human knee. By integrating a micro linear motor into the piston rod of an MR damper, the LMRA combines the active mode and the semi-active mode, enabling it to output driving force in the active mode and controllable damping force in the semi-active mode. The remainder of this paper is organized as follows. Section 2 introduces the structures and working principles of the SCMRPK and the LMRA. Section 3 presents the key dimensional design method for the LMRA magnetic circuit. Section 4 provides simulation and experimental verification of the damping-force characteristics of the MR damper in the semi-active mode of the LMRA. Section 5 establishes the kinematic and dynamic models of the SCMRPK-based lower limb prosthesis. Section 6 presents the control methods of the SCMRPK in the semi-active and active modes. Section 7 experimentally evaluates the displacement

https://doi.org/10.1017/S0263574726103610 Published online by Cambridge University Press

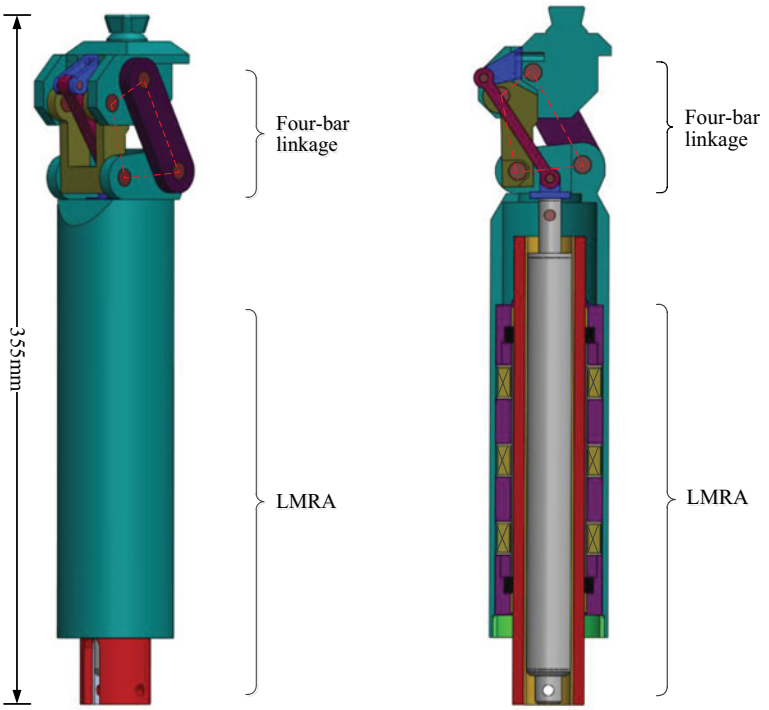


Figure 2. *SCMRPK: (a) the three-dimensional structure and (b) the three-dimensional sectional view.*

tracking performance of the LMRA in active mode. Section 8 presents the semi-active gait experiments and active obstacle-crossing experiments of the SCMRPK.

2. Principle and structure

Figure 2(a) and (b) show the three-dimensional structure and sectional view of the SCMRPK, respectively. The SCMRPK mainly consists of a four-bar linkage mechanism and the LMRA. The upper link and the lower link of the four-bar linkage are connected to the piston rod and the outer cylinder of the LMRA, respectively. This design realizes the integrated configuration of the LMRA and the four-bar linkage. The SCMRPK prototype has an overall height of 355 mm, a length of 60 mm, and a width of 53 mm. Compared with the knee-joint structural dimensions of the other active lower limb assistive devices listed in Table I, the SCMRPK has a more compact knee-joint structure. As shown in Figure 3, the overall dimensions of the integrated SCMRPK are controlled within the dimensional range of the natural human lower limb.

Figure 4 shows the principle of the proposed LMRA, and Figure 5(a) and (b) show its three-dimensional structure and sectional view, respectively. The LMRA consists of an MR damper and a micro linear motor. The MR damper is a double-rod damper, and the micro linear motor is integrated into the piston rod of the damper to form an integrated design.

Figure 6 shows the structural schematic of the LMRA. The MR damper mainly consists of a piston tube, an inner cylinder, and an outer cylinder. The inner cylinder includes an upper lid, a lower lid, four magnetic disks, two sealing rings, and three bobbins with wound coils and is firmly fixed inside the outer cylinder. The MR damper used in this study operates in shear mode. MRF fills the fluid gap between the inner cylinder and the piston tube and generates yield shear stress under the excitation current, thereby producing controllable damping force during relative motion. Therefore, the damping

https://doi.org/10.1017/S0263574726103610 Published online by Cambridge University Press

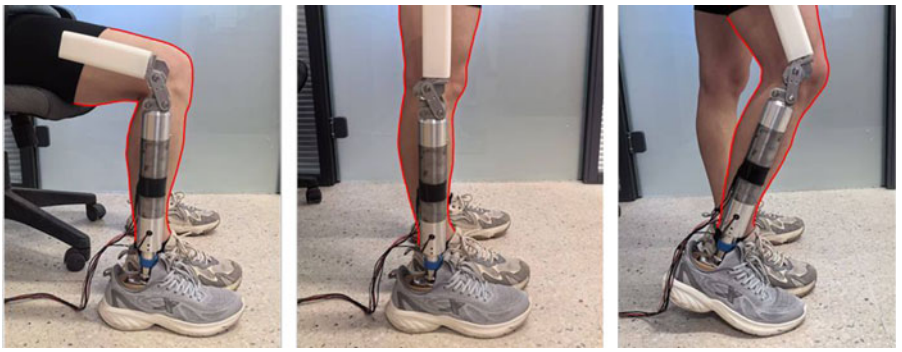


Figure 3. *Comparison of the SCMRPK with the human lower limb.*

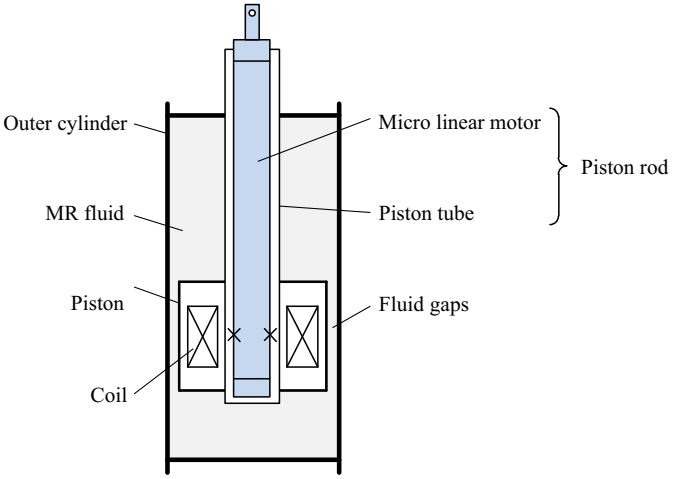


Figure 4. *Principle of the LMRA.*

force is mainly determined by the excitation current and the relative velocity. The micro linear motor consists of a telescopic pole and a motor base. A lead screw-nut mechanism is adopted inside the motor: the DC motor drives the nut to rotate, thereby driving the telescopic pole to extend and retract. The motor is packaged inside the piston tube and, together with the piston tube, forms the piston rod. The LMRA adopts a three-stage series structure, and the primary structure is indicated by the dashed box in Figure 6. The piston tube, magnetic disks, and outer cylinder are made of 20# steel for high permeability, and the bobbins with wound coils are made of 304 steel for low permeability. Therefore, when the coils are energized, a closed magnetic circuit is formed, and the magnetic flux passes successively through the piston tube, the fluid gap, the magnetic disks, and the outer cylinder. To avoid interference of the damper magnetic field with the micro linear motor, a brass isolation tube is arranged between the motor and the piston tube. It should be noted that this structural principle is also applicable to general linear MR dampers.

Figures 7 and 8 show the working principles of the SCMRPK in the semi-active mode and the active mode, respectively. Figures 7(a) and 8(a) show the overall motion states of the four-bar prosthetic knee joint in the two modes, respectively. In the semi-active mode, the DC motor is powered off, and the screw-nut mechanism is in a self-locking state so that no relative motion occurs between the telescopic pole and the motor base. At this time, the piston rod moves within the inner cylinder, and its relative displacement is regulated by the damping force. As shown in Figure 7(b), the white double-headed

https://doi.org/10.1017/S0263574726103610 Published online by Cambridge University Press

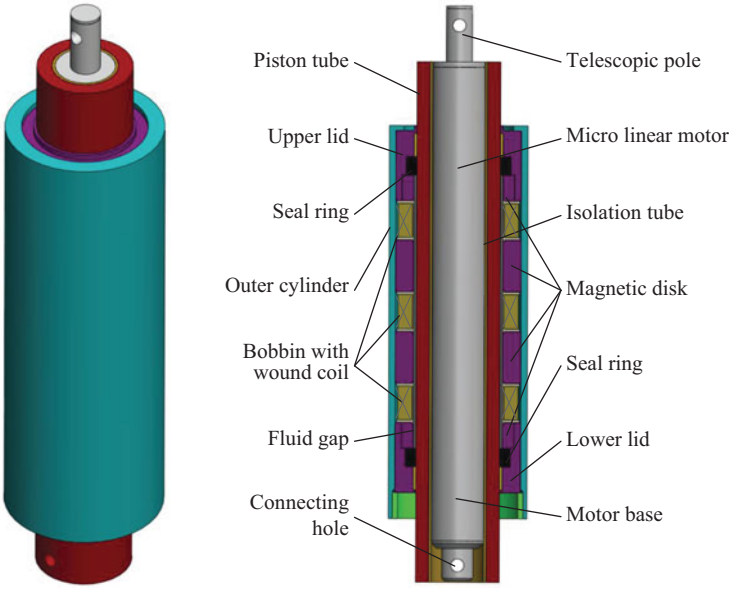


Figure 5. *LMRA: (a) the three-dimensional structure and (b) the three-dimensional sectional view.*

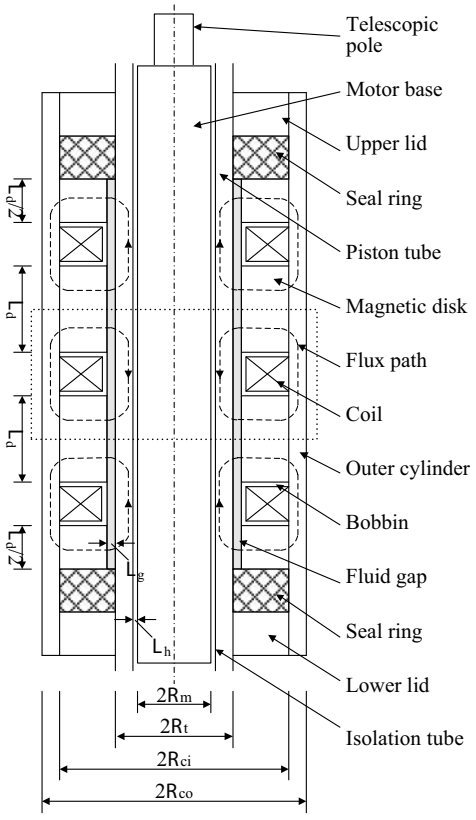


Figure 6. *Structural schematic diagram of the LMRA.*

https://doi.org/10.1017/S0263574726103610 Published online by Cambridge University Press

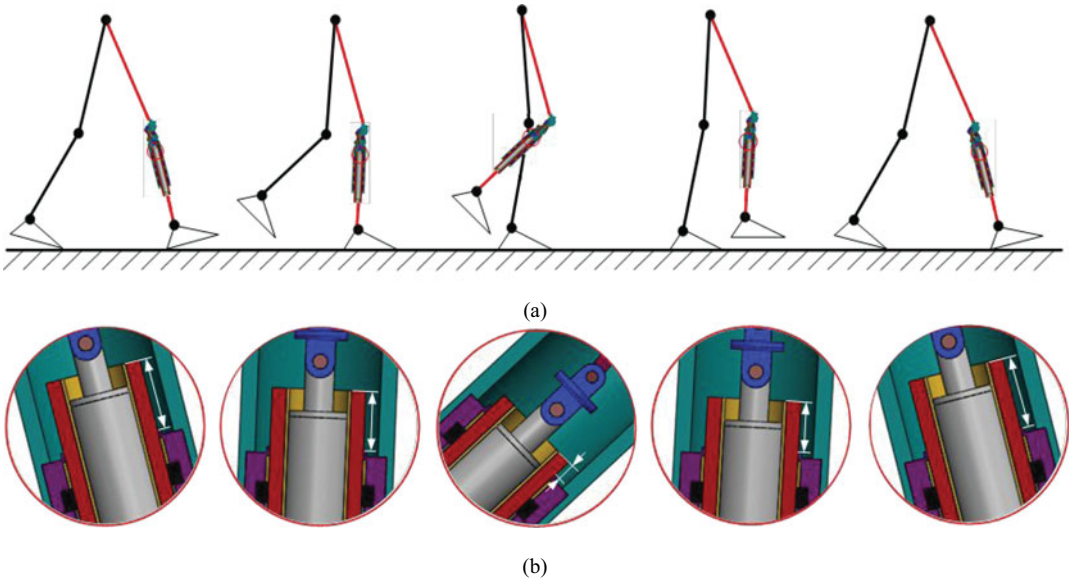


Figure 7. *SCMRPK in semi-active mode: (a) the motion of the entire four-bar prosthesis and (b) the motion of LMRA.*

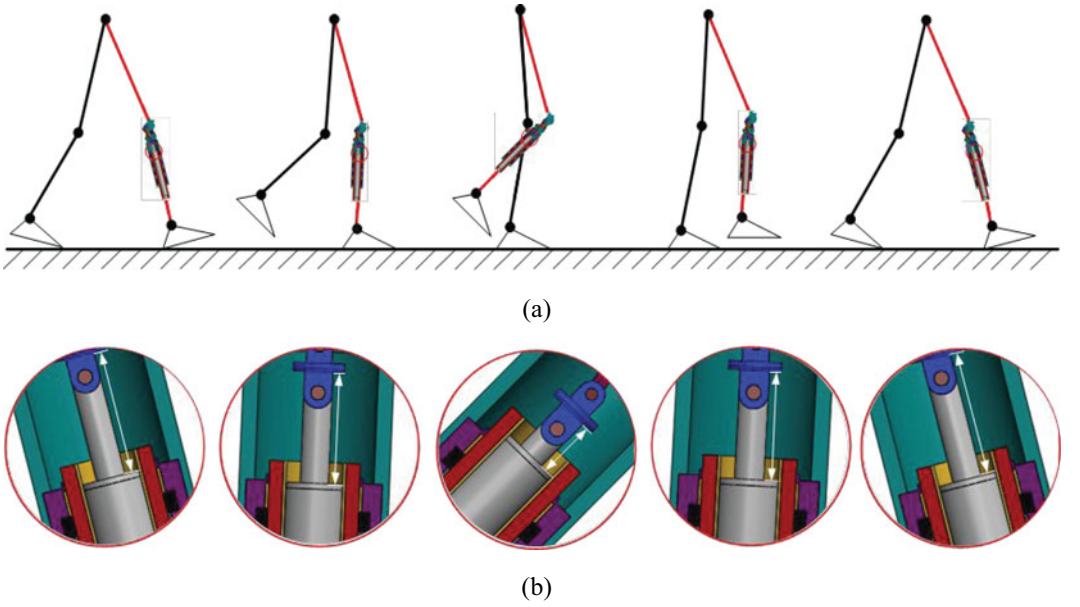


Figure 8. *SCMRPK in active mode: (a) the motion of the entire four-bar prosthesis and (b) the motion of LMRA.*

arrow indicates the relative displacement between the piston tube and the inner cylinder. By changing the coil current, the damping force of the MR damper can be adjusted, thereby controlling the motion of the four-bar linkage and driving the prosthetic knee joint to the desired angle. In the active mode, a locking current is applied to the coils, and the damper outputs a large damping force so that no relative motion occurs between the piston tube and the inner cylinder. At this time, the DC motor drives the screw-nut mechanism to move the telescopic pole. As shown in Figure 8(b), the white double-headed

https://doi.org/10.1017/S0263574726103610 Published online by Cambridge University Press

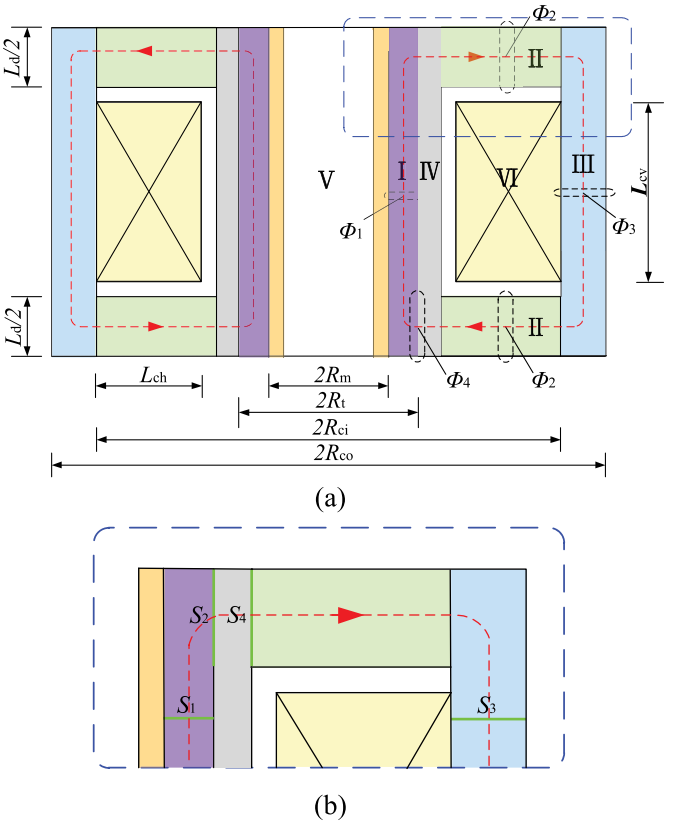


Figure 9. *Primary structure of the MR damper: (a) overall figure. (b) local figure.*

arrow indicates the relative displacement between the tip of the telescopic pole and the motor base. The motion of the telescopic pole drives the four-bar linkage, thereby moving the prosthetic knee joint to the desired angle.

3. Design of the LMRA magnetic circuit

Since the LMRA consists of three identical primary structures, the dimensional design only needs to be carried out for a single structure. To ensure that the directions of the excitation magnetic fields are consistent in all structures, the winding directions of the coils in adjacent structures are opposite. In this section, a practical dimensional design method is adopted to determine the structural parameters of the MR damper. As shown in Figure 9, the primary structure of the LMRA is divided into six regions: region I is the piston tube, region II is the magnetic disk, region III is the outer cylinder, region IV is the MRF, region V is the micro linear motor, and region VI is the excitation coil; Φ_1, Φ_2, Φ_3, and Φ_4 represent the magnetic fluxes in regions I to IV, respectively. It should be noted that the micro linear motor is separated from the magnetic circuit design region by an isolation tube.

The aim of the dimensional design is to maximize the damping force of the MR damper. To achieve this goal, the main working regions in the magnetic circuit of the primary structure should approach magnetic saturation as simultaneously as possible, while the coil turns are properly matched.

The magnetic circuit of the primary structure is shown by the red dashed line in Figure 9, passing through region I, region IV, region II, region III, region II, region IV, and finally returning to region I. The series magnetic flux Φ is equal everywhere, which is given by

$$\Phi_1 = \Phi_2 = \Phi_3 = \Phi_4 \tag{1}$$

https://doi.org/10.1017/S0263574726103610 Published online by Cambridge University Press

Table II. *Dimensional parameters and material properties of the primary structure of the MR damper.*

Parameter	Symbol	Calculated value	Basic value
Radius of the isolation tube	R_m	11 mm	11 mm
Radius of the piston rod	R_t	15.4 mm	16 mm
Height of the magnetic disk	L_d	20 mm	20 mm
Fluid gap width	L_g	1 mm	1 mm
Radius of the inner cylinder	R_{ci}	24.2 mm	24 mm
Radius of the outer cylinder	R_{co}	26.5 mm	26.5 mm
Length of the turns of the coil	L_{cv}	14 mm	14 mm
Number of the turns of the coil	N		150
Current	I		0–2.4 A
Material of the bobbin			304 steel
Material of the isolation tube			brass
Material of the rest			20# steel

As shown in Figure 9, the cross-sectional areas of regions I, II, III, and IV in the magnetic circuit vary along the magnetic path. To allow the main working regions in the magnetic circuit to approach magnetic saturation as simultaneously as possible, the minimum cross-sectional area of each of the four regions is designated as the effective cross-sectional area for that region. According to the law of magnetic flux conservation, the magnetic flux of the circuit is given as follows:

$$\Phi = B_i S_i \tag{2}$$

where B_i denotes the magnetic flux density in region i, and S_i denotes the corresponding effective cross-sectional area.

In the magnetic circuit shown in Figure 9, regions I, II, and III are made of 20# steel, while region IV is filled with MRF. The saturation magnetic flux density of 20# steel is denoted by B_M (about 1.6 T), whereas the magnetic flux density corresponding to the saturated yield stress of the MRF is denoted by B_F (about 0.6 T). To allow the main working regions with different materials to approach magnetic saturation as simultaneously as possible, the effective cross-sectional areas of these regions should be properly allocated. Since the magnetic circuit passes through the MRF and then the 20# steel, and the adjacent regions have similar cross-sectional areas, the MRF region reaches saturation more easily, thereby limiting the further increase in magnetic flux density in the adjacent 20# steel regions. Therefore, the area S_4 of the MRF region should be determined first, followed by the areas S_1 and S_3 of the 20# steel regions that can reach saturation, and finally S_2. The effective cross-sectional areas of all regions are used to determine the calculated dimensional parameters of the primary structure of the LMRA, while the actual dimensions are determined according to manufacturing and assembly requirements. The structural parameters and material properties of the LMRA are listed in Table II.

According to Table II, the maximum magnetic flux in each region can be calculated using Eq. (2) as follows:

$$\Phi_{1s} = B_M S_1 = B_M \times \pi \left[R_t^2 - R_m^2\right] = 678.24 \tag{3}$$

$$\Phi_{2s} = B_F S_2 = B_F \times \pi \left(R_t + h\right) L_d = 640.56 \tag{4}$$

$$\Phi_{3s} = B_M S_3 = B_M \times \pi \left[R_{co}^2 - R_{ci}^2\right] = 634.28 \tag{5}$$

$$\Phi_{4s} = B_F S_4 = B_F \times \pi R_t L_d = 602.88 \tag{6}$$

where Φ_{1s}, Φ_{2s}, Φ_{3s}, and Φ_{4s} represent the maximum magnetic flux in regions I, II, III, and IV, respectively. Once the magnetic flux in a region reaches its maximum value, it no longer increases. Based on

https://doi.org/10.1017/S0263574726103610 Published online by Cambridge University Press



(a) (b)

Figure 10. *Photographs of the LMRA prototype: (a) components and (b) assembled actuator.*

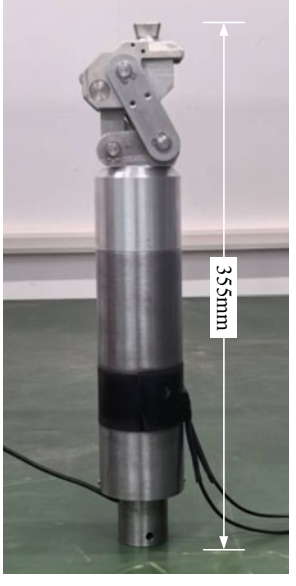


Figure 11. *Photograph of the SCMRPK prototype.*

the above calculation results, when region IV, which has the smallest maximum magnetic flux, reaches magnetic saturation, regions I and III also approach saturation almost simultaneously.

After the magnetic flux distribution in the magnetic circuit has been determined, the number of turns of the coil can be obtained according to Kirchhoff's law for magnetic circuits:

$$NI = \Phi \sum R \tag{7}$$

where n is the number of turns of the excitation coil, I is the excitation current on the coil, and $\sum R$ is the total reluctance of the magnetic circuit. According to Eq. (7), the number of turns n of the coil is approximately 150. The LMRA prototype is shown in Figure 10, and the SCMRPK prototype developed on this basis is shown in Figure 11.

https://doi.org/10.1017/S0263574726103610 Published online by Cambridge University Press

Table III. *The magnetic flux density of each sampling point under different currents.*

Point	0.4 A	0.8 A	1.2 A	1.6 A	2.0 A	2.4 A
A	0.37133 T	0.69420 T	0.98897 T	1.24933 T	1.43514 T	1.57529 T
B	0.37725 T	0.70552 T	1.00564 T	1.27304 T	1.47004 T	1.62692 T
C	0.14022 T	0.26135 T	0.37160 T	0.46957 T	0.54199 T	0.59952 T

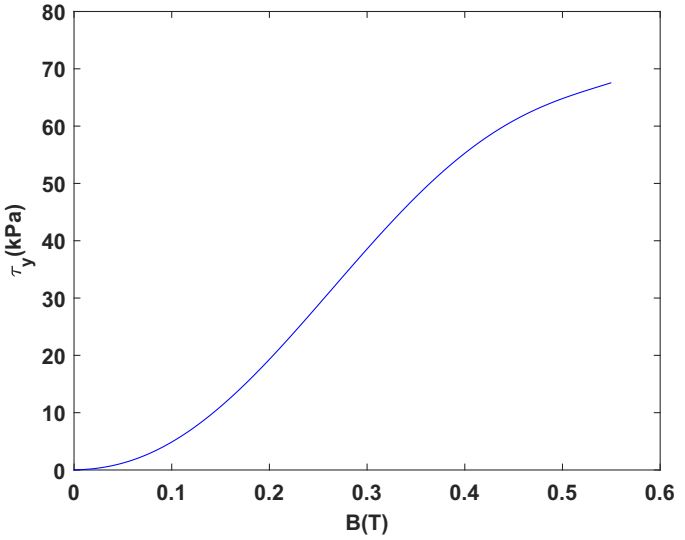


Figure 12. *Yield stress (τ_y) as a function of magnetic flux density (B) of the MRJ-01.*

4. Simulation and experiment of the LMRA in semi-active mode

According to the Bingham model [43], the damping force (F_d) of the MR damper can be represented as

$$F_d = F_s^{\eta} + F_s^{\tau}\mathrm{sgn}\left(\Delta\dot{d}\right) = \frac{3\eta\Delta\dot{d}L_d w}{L_g} + 3\tau_y(B)L_d w\mathrm{sgn}\left(\Delta\dot{d}\right) \tag{8}$$

where $F_s{}^{\eta}$ is the initial viscosity of the MRF, $F_s{}^{\tau}$ is the yield stress controlled by the external magnetic field intensity, η is the post-yield viscosity of the MRF, $\Delta\dot{d}$ is the relative velocity between the piston tube and the inner cylinder, w ($=2\pi(R_t+L_g/2)$) is the expanded length of the fluid gap, $\tau_y(B)$ is the field-dependent yield stress, B is the magnetic flux density of the external magnetic field in the fluid gap, and sgn(.) is the signum function.

According to Figure 12, the relationship between the yield stress $\tau_y(B)$ of the MRF (type:MRJ-01) and the magnetic flux density B can be expressed as follows

$$\tau_y(B) = a_{y5}B^5 + a_{y4}B^4 + a_{y3}B^3 + a_{y2}B^2 + a_{y1}B + a_{y0} \tag{9}$$

where $a_{y5} = 4.583 \times 10^3$ kPa/T^5, $a_{y4} = -5.700 \times 10^3$ kPa/T^4, $a_{y3} = 1.486 \times 10^3$ kPa/T^3, $a_{y2} = 3.630 \times 10^2$ kPa/T^2, $a_{y1} = 2.628$ kPa/T, and $a_{y0} = 2.100 \times 10^{-2}$ kPa.

Figure 13 shows the magnetic flux density distribution in the fluid gap (region IV) under the maximum current excitation of 2.4 A. Sampling points A, B, and C are located at the middle positions of regions I, III, and IV, respectively, and are used to represent the magnetic flux densities in these regions. The magnetic flux densities at the sampling points under different current excitations are listed in Table III. The results show that the magnetic flux density in each region gradually increases with current and approaches saturation at 2.4 A.

https://doi.org/10.1017/S0263574726103610 Published online by Cambridge University Press

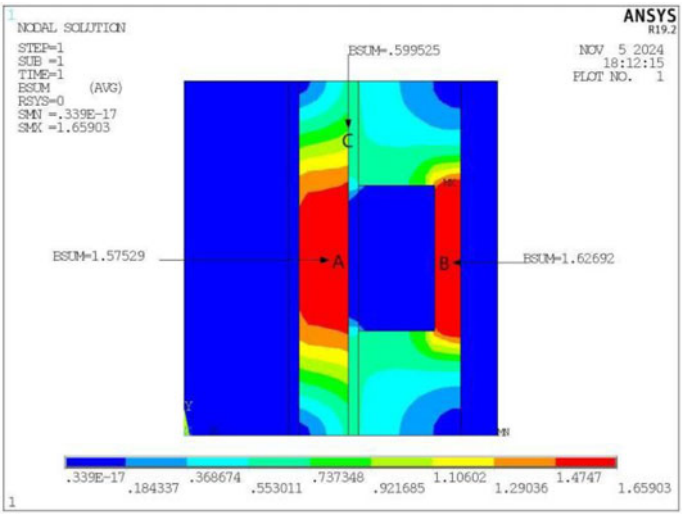


Figure 13. *The contour of magnetic flux density (values in T) under a 2.4 A current excitation.*

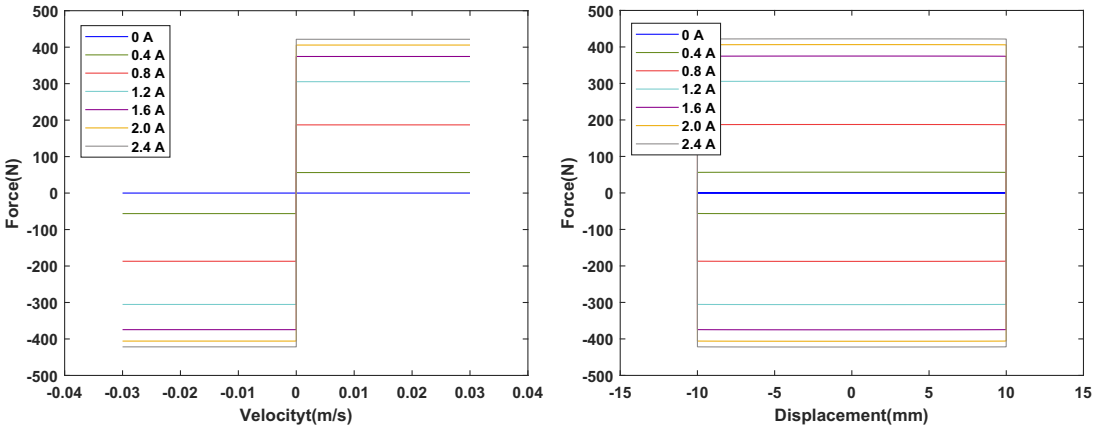


Figure 14. *Calculated damping forces of the integrated MR damper under a 0.5 Hz sinusoidal displacement excitation with an amplitude of 10 mm: (a) the force versus velocity and (b) the force versus displacement.*

According to Figure 13 and Table III, the relationship between the magnetic flux density in the fluid gap and the excitation current can be expressed as follows:

$$B = f(I) = b_2 I^2 + b_1 I + b_0 \tag{10}$$

where $b_2 = -5.794 \times 10^{-2}$, $b_1 = 0.3716$, $b_0 = -3.695 \times 10^{-3}$.

According to Eq. (8)–(10), adjusting the current in the excitation coil changes the magnetic flux density in the fluid gap and thereby produces a controllable damping force in the MR damper. In the semi-active mode, the LMRA can be regarded as an MR damper. The damping-force characteristics of the MR damper under different excitation conditions can therefore be calculated from Eq. (8)–(10). Figure 14 shows the calculated results under a 0.5 Hz sinusoidal displacement excitation with an amplitude of 10 mm. The calculated results show that the damping force reaches about 421 *n* at 2.4 A. To obtain damping-force data closer to the actual values, the MR damper was tested using a shock testing machine

https://doi.org/10.1017/S0263574726103610 Published online by Cambridge University Press

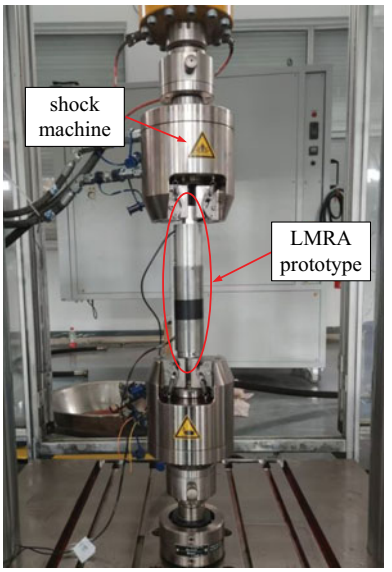


Figure 15. *Experimental setup for the semi-active mode experiment of LMRA.*

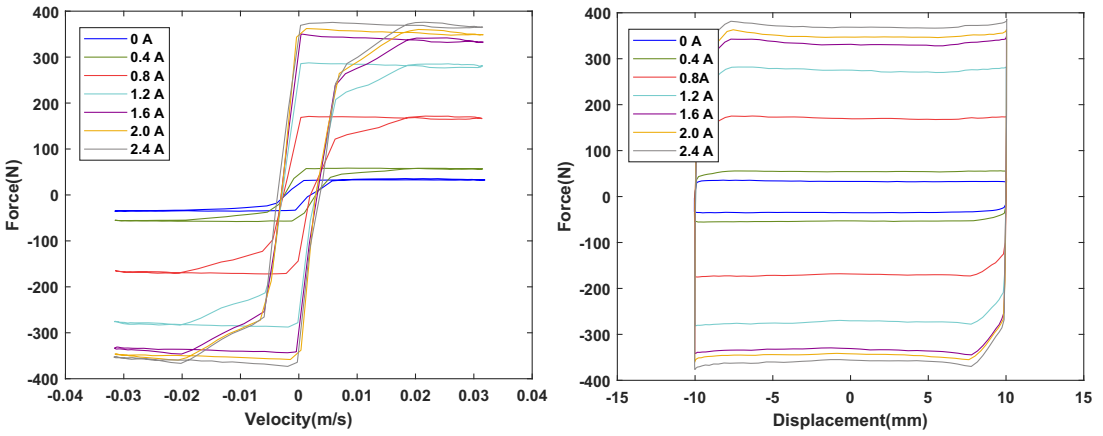
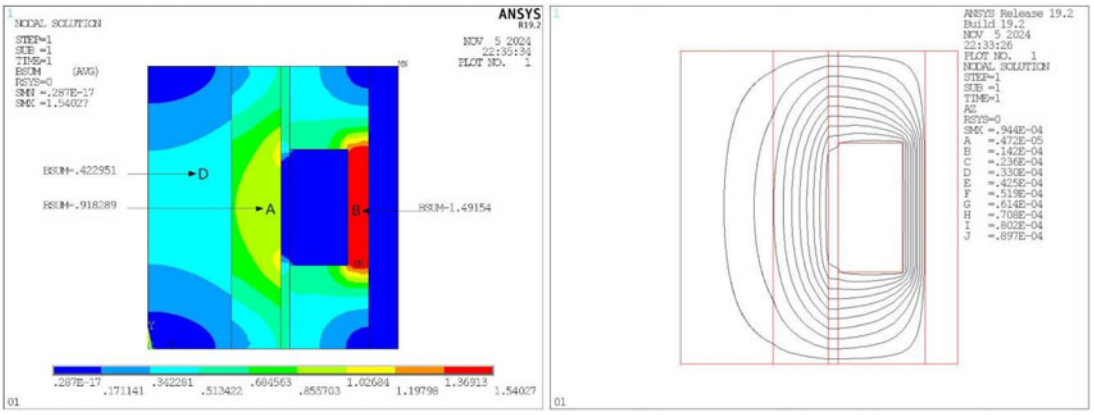


Figure 16. *Measured damping forces of the integrated MR damper under a 0.5 Hz sinusoidal displacement excitation with an amplitude of 10 mm: (a) the force versus velocity and (b) the force versus displacement.*

(LFV-50.HH, Walter+Bai AG), and the experimental setup is shown in Figure 15. Figure 16 shows the measured results under the same excitation conditions. The measured damping force reaches about 367 *n* at 2.4 A. The measured results are slightly lower than the calculated results, mainly because the MRF cannot completely fill the cavity and perfect sealing is difficult to achieve in the experiment. Therefore, some deviation exists between the experimental and simulation results. These results demonstrate that the dimensional design method adopted for the LMRA is effective.

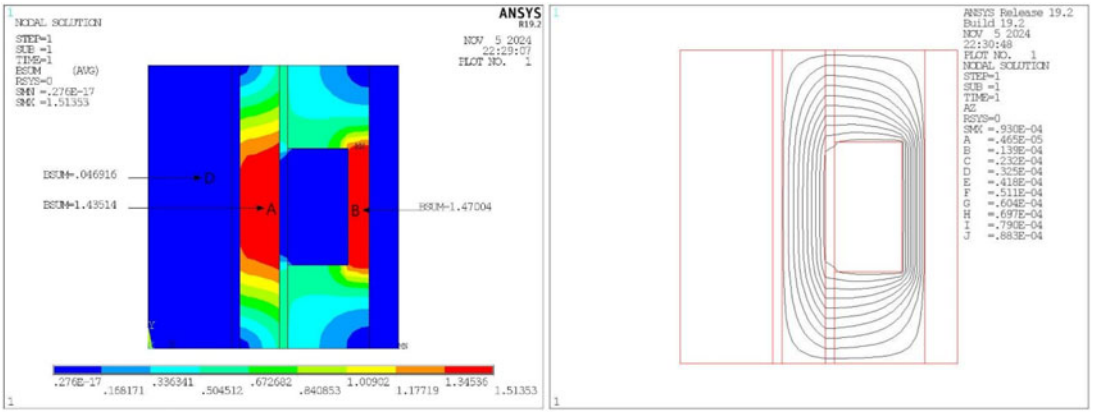
To suppress the influence of the damper magnetic field on the micro linear motor, a 1 mm thick brass isolation tube was arranged between the motor and the piston tube. As shown in Figures 17 and 18, comparative simulations were carried out for the two structures with and without the isolation tube under the 2.0 A condition. The simulation results show that, without the isolation tube, part of the

https://doi.org/10.1017/S0263574726103610 Published online by Cambridge University Press



(a) (b)

Figure 17. *Finite element method analysis of the LMRA without isolation tube: (a) Contour of magnetic flux density (values in T) and (b) Magnetic flux distribution.*



(a) (b)

Figure 18. *Finite element method analysis of the LMRA with isolation tube: (a) Contour of magnetic flux density (values in T) and (b) Magnetic flux distribution.*

magnetic flux lines enters the motor region and may affect its normal operation. After the isolation tube is introduced, the magnetic flux lines are effectively confined within the designed magnetic circuit, and the magnetic flux density in the motor region is significantly reduced. This indicates that the isolation tube can effectively isolate magnetic field interference and satisfies the structural design requirements.

5. Kinematic and dynamic modeling of the SCMRPK

As shown in Figure 19, the SCMRPK-based lower limb prosthesis consists of the SCMRPK prototype, a prosthetic shank, and a prosthetic foot. The thigh synchronization mechanism (TSM) is affixed to the test subject's thigh and moves synchronously with it through restraint. The prosthesis is installed at the knee joint of the subject using a specially designed connector located at the lower end of the TSM.

The normal gait cycle consists of the stance and swing phases. Since prosthetic knee joints based on four-bar linkage mechanisms can achieve stability in the stance phase through self-regulation [44, 45], this paper focuses on the kinematic characteristics of the SCMRPK in the swing phase.

https://doi.org/10.1017/S0263574726103610 Published online by Cambridge University Press

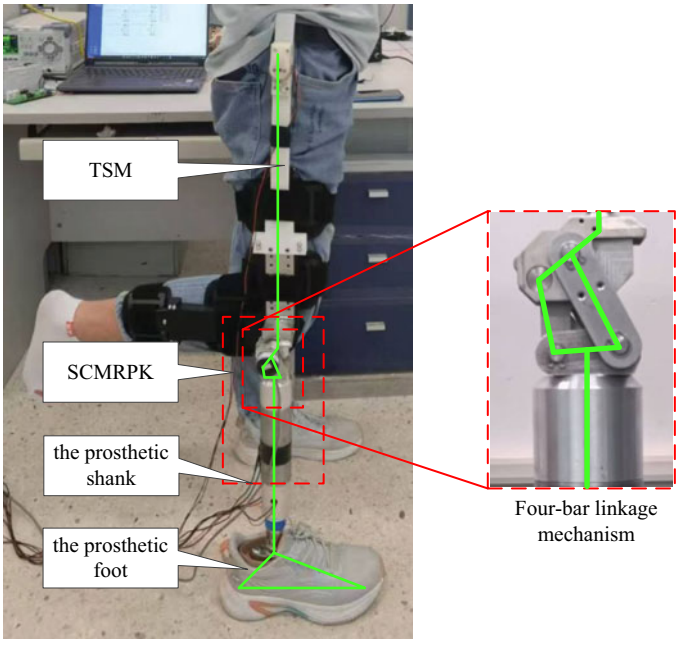


Figure 19. *The photograph of the SCMRPK-based lower limb prosthesis.*

As shown in Figure 20, the point o represents the hip joint; the point K_j represents the jth ($j = 1,\ldots,4$) axis of the four-bar linkage; the point n represents the intersection point of the fourth and sixth link rods; the second, third, fifth, and sixth link rods represent the front, back, upper, and lower link rods, respectively; the first link rod represents the thigh; the fourth link rod represents the shank; the point P_i represents the center of mass of the ith ($i = 1,\ldots,4$) link rod.

According to Lagrange's second kinetic equation, the governing equation of the lower limb prosthesis in the swing phase is given by

$$\begin{cases} L = \sum_{i=1}^{4} (E_i - V_i) = \sum_{i=1}^{4} \left[\frac{1}{2} m_i \left(\dot{x}_i^2 + \dot{y}_i^2 \right) + \frac{1}{2} J_i \dot{\theta}_i^2 - m_i g y_i \right] \\ \begin{bmatrix} 1 & -1 & -1 & 0 \\ 0 & 1 & 0 & -1 \\ 0 & 0 & 1 & -1 \\ 0 & 0 & 0 & 1 \end{bmatrix} \begin{bmatrix} T_1 \\ T_2 \\ T_3 \\ T_4 \end{bmatrix} = \begin{bmatrix} \frac{d}{dt}\left(\frac{\partial L}{\partial \dot{\theta}_1}\right) - \frac{\partial L}{\partial \dot{\theta}_1} \\ \frac{d}{dt}\left(\frac{\partial L}{\partial \dot{\theta}_2}\right) - \frac{\partial L}{\partial \dot{\theta}_2} \\ \frac{d}{dt}\left(\frac{\partial L}{\partial \dot{\theta}_3}\right) - \frac{\partial L}{\partial \dot{\theta}_3} \\ \frac{d}{dt}\left(\frac{\partial L}{\partial \dot{\theta}_4}\right) - \frac{\partial L}{\partial \dot{\theta}_4} \end{bmatrix} \\ = \begin{bmatrix} M_{11} & M_{12} & M_{13} & M_{14} \\ M_{21} & M_{22} & M_{23} & M_{24} \\ M_{31} & M_{32} & M_{33} & M_{34} \\ M_{41} & M_{42} & M_{43} & M_{44} \end{bmatrix} \begin{bmatrix} \ddot{\theta}_1 \\ \ddot{\theta}_2 \\ \ddot{\theta}_3 \\ \ddot{\theta}_4 \end{bmatrix} + \begin{bmatrix} C_1 \\ C_2 \\ C_3 \\ C_4 \end{bmatrix} + \begin{bmatrix} G_1 \\ G_2 \\ G_3 \\ G_4 \end{bmatrix} \end{cases} \tag{11}$$

where L is the Lagrange function of the multi-rigid-body system; E_i is the kinetic energy of the ith link rod; V_i is the potential energy of the ith link rod; θ_i is the relative angle between the ith link rod and

https://doi.org/10.1017/S0263574726103610 Published online by Cambridge University Press

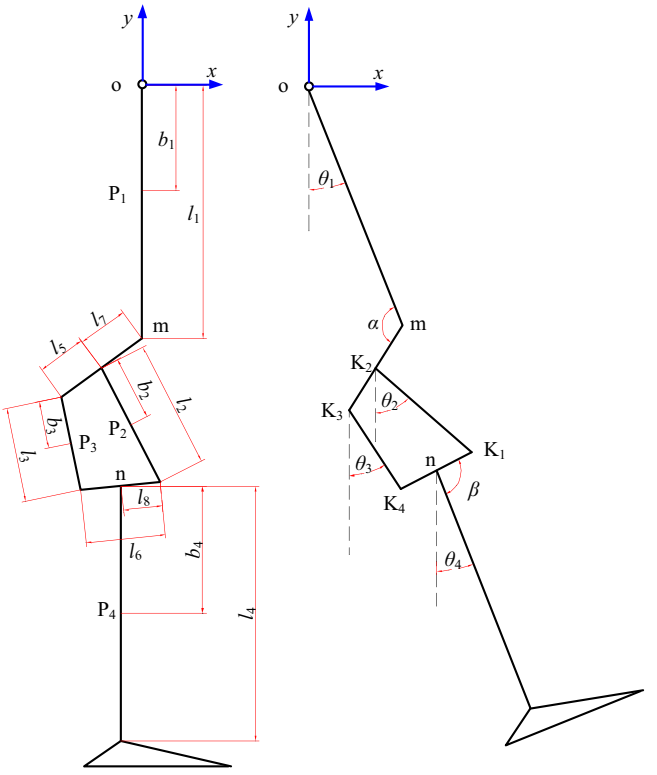


Figure 20. *Equivalent diagram of the lower limb prosthesis.*

the vertical direction; x_i is the horizontal coordinate of the point P_i; y_i is the vertical coordinate of the point P_i; m_i is the mass of the ith link rod; J_i is the moment of inertia of the ith link rod; T_i is the generalized torque corresponding to θ_i; M_{ij} is a component of the inertia matrix; C_i is a component of the centripetal and Coriolis torque matrix; and G_i is a component of the gravitational torque and hip acceleration matrix.

Considering that the four-bar linkage is a closed-loop structure, the constraint equation about Eq. (11) is given by

$$\begin{cases} l_5 \cos\left(\frac{\pi}{2}+\alpha+\theta_1\right)+l_2\cos\left(\frac{\pi}{2}+\theta_2\right)=l_3\cos\left(\frac{\pi}{2}+\theta_3\right)+l_6\cos\left(\frac{\pi}{2}+\beta+\theta_4\right) \\ l_5 \sin\left(\frac{\pi}{2}+\alpha+\theta_1\right)+l_2\sin\left(\frac{\pi}{2}+\theta_2\right)=l_3\sin\left(\frac{\pi}{2}+\theta_3\right)+l_6\sin\left(\frac{\pi}{2}+\beta+\theta_4\right) \end{cases} \tag{12}$$

where l_i is the length of the ith ($i=1,\ldots,8$) link rod; α is the angle between the first link rod and the seventh link rod; and β is the angle between the fourth link rod and the sixth link rod.

According to Eq. (11), when $T_3=0$ and $T_4=0$, the torque (T_2) around the axis K_2 is given by

$$T_2=\frac{d}{dt}\left(\frac{\partial L}{\partial \dot{\theta}_2}\right)-\frac{\partial L}{\partial \dot{\theta}_2}=M_{21}\ddot{\theta}_1+M_{22}\ddot{\theta}_2+M_{23}\ddot{\theta}_3+M_{24}\ddot{\theta}_4+C_2+G_2 \tag{13}$$

where M_{21}, M_{22}, M_{23}, M_{24}, C_2, G_2, and J_2 are governed by

$$\begin{aligned} M_{21}=&m_2l_7b_2\sin\alpha\sin(\theta_1-\theta_2)-m_2b_2(l_7\cos\alpha-l_1)\cos(\theta_1-\theta_2)\\ &+m_4l_2l_7\sin\alpha\sin(\theta_1-\theta_2)-m_4l_2(l_7\cos\alpha-l_1)\cos(\theta_1-\theta_2) \end{aligned}$$

$$M_{22}=J_2+m_2b_2^2+m_4l_2^2$$

https://doi.org/10.1017/S0263574726103610 Published online by Cambridge University Press

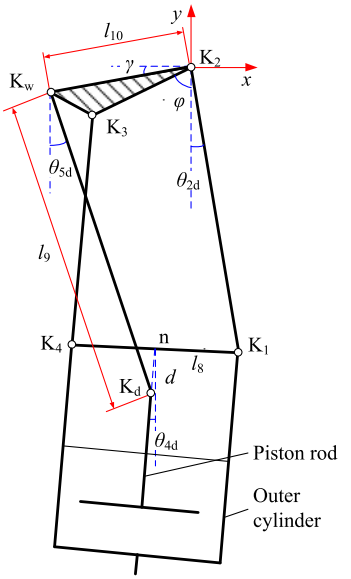


Figure 21. *Equivalent diagram of the SCMRPK when θ_1 is equal to 0.*

$$M_{23} = 0$$

$$M_{24} = m4l_2b_4\cos(\theta_4 - \theta_2) - m_4l_2l_8\cos(\theta_4 - \theta_2 + \beta)$$

$$C_2 = \begin{bmatrix} m_2l_7b_2\sin\alpha\cos(\theta_1 - \theta_2) + m_2b_2(l_7\cos\alpha - l_1)\sin(\theta_1 - \theta_2) \\ +m_4l_2l_7\sin\alpha\cos(\theta_1 - \theta_2) + m_4l_2(l_7\cos\alpha - l_1)\sin(\theta_1 - \theta_2) \end{bmatrix}\dot{\theta}_1^2 + [m_4l_2l_8\sin(\theta_4 - \theta_2 + \beta) - m_4l_2b_4\sin(\theta_4 - \theta_2)]\dot{\theta}_4^2$$

$$G_2 = (m_2b_2\cos\theta_2 + m_4l_2\cos\theta_2)\ddot{x}_o + (m_2b_2\sin\theta_2 + m_4l_2\sin\theta_2)\ddot{y}_o + m_2gb_2\sin\theta_2 + m_4gl_2\sin\theta_2$$

$$J_2 = m_2b_2^2/12$$

where (x_o, y_o) is the coordinate of the point o; g ($g = 9.8$) is the gravity; b_1 is the distance from the point o to the point P_1; b_2 is the distance from the point K_2 to the point P_2; b_3 is the distance from the point K_3 to the point P_3; and b_4 is the distance from the point n to the point P_4.

As shown in Figure 2(b), the actuating mechanism of the SCMRPK is the LMRA, which generates the torque (T_2) around the axis K_2. The damping force of the MR damper (F_{damper}) is determined by the relative velocity between the piston rod and the inner cylinder and the current in the coils. The relative velocity between the piston rod and the inner cylinder, as well as the coil current, is independent of θ_1.

Figure 21 shows the equivalent diagram of the SCMRPK when θ_1 is equal to 0. K_d and K_w denote the hinge points between the piston rod and the swing link and between the thigh connector and the swing link, respectively. The ninth link rod represents the swing link rod, and the triangle $K_wK_2K_3$ represents the thigh connector. According to the virtual work principle, the relationship between the torque (T_2) around the axis K_2 and the F_{damper} in the direction of the piston rod is given by

$$T_2\delta\theta_{2d} = F_{\text{damper}}\delta d \tag{14}$$

where d is the distance from the point K_d to the sixth link rod in the direction of the piston rod; θ_{2d} is the angle between the second link rod and the vertical direction when θ_1 is equal to 0; $\delta\theta_{2d}$ is the virtual displacement of θ_{2d}; and δ_d is the virtual displacement of d.

https://doi.org/10.1017/S0263574726103610 Published online by Cambridge University Press

Considering the closed-loop path ($K_2K_wK_dnK_1K_2$) as shown in Figure 20, the constraint equation about Eq. (14) is given by

$$\begin{cases} l_2\cos\left(\frac{\pi}{2}+\theta_{2d}\right)+l_{10}\cos(\pi+\gamma)+d\cos\left(\frac{\pi}{2}+\theta_{4d}\right)=l_9\cos\left(\frac{\pi}{2}+\theta_{5d}\right)+l_8\cos\left(\frac{\pi}{2}+\beta+\theta_{4d}\right) \\ l_2\sin\left(\frac{\pi}{2}+\theta_{2d}\right)+l_{10}\sin(\pi+\gamma)+d\sin\left(\frac{\pi}{2}+\theta_{4d}\right)=l_9\sin\left(\frac{\pi}{2}+\theta_{5d}\right)+l_8\sin\left(\frac{\pi}{2}+\beta+\theta_{4d}\right) \end{cases} \tag{15}$$

where l_i is the length of the ith ($i=9$, 10) link rod; γ is the angle between the tenth link rod and the horizontal direction; θ_{4d} is the angle between the fourth link rod and the vertical direction when θ_1 is equal to 0; and θ_{5d} is the angle between the ninth link rod and the vertical direction when θ_1 is equal to 0.

According to Figures 20 and 21, the relative angle (θ_{4d}) between the thigh and the shank, which is the knee angle of the SCMRPK, is

$$\theta_{4d}=\theta_4-\theta_1 \tag{16}$$

The relative angle (θ_{2d}) between the second link rod and the vertical direction is

$$\theta_{2d}=\theta_2-\theta_1 \tag{17}$$

where φ is the angle between the fifth link rod and the vertical direction when θ_1 is equal to 0.

According to Eqs. (12) and (15), the relationship between θ_{4d} and θ_{2d} is

$$\begin{aligned} \theta_{4d}=\arcsin&\frac{l_2^{\,2}+l_5^{\,2}+l_6^{\,2}-l_3^{\,2}+2l_2l_5\cos(\theta_{2d}-\alpha)}{-2l_6\sqrt{l_2^{\,2}+l_5^{\,2}+2l_2l_5\cos(\theta_{2d}-\alpha)}} \\ &+\operatorname{arctg}\frac{l_5\sin(\alpha)+l_2\sin(\theta_{2d})}{l_5\cos(\alpha)+l_2\cos(\theta_{2d})}-\beta+\frac{\pi}{2} \end{aligned} \tag{18}$$

According to Eq. (15), the displacement (Δd) of K_d in the direction of the piston rod is

$$\begin{aligned} \Delta d=&\,l_8\cos\beta-l_2\cos(\theta_{2d}-\theta_{4d})-l_{10}\sin(\theta_{4d}-\gamma)-d_0 \\ &+\sqrt{\begin{array}{l} l_9^2-l_2^2-l_{10}^2-l_8^2+2l_8l_{10}\sin(\beta+\theta_{4d}-\gamma)-2l_2l_{10}\sin(\theta_{2d}-\gamma) \\ +2l_2l_8\cos(\beta+\theta_{4d}-\theta_{2d})+(l_2\cos(\theta_{2d}-\theta_{4d})+l_{10}\sin(\theta_{4d}-\gamma)-l_8\cos\beta)^2 \end{array}} \end{aligned} \tag{19}$$

where d_0 is the initial length of the telescopic pole, $\theta_{4d}=0$.

Based on the established dynamic model, Figure 22 shows the time-history curve of the damping force required from the MR damper during the swing phase of the prosthetic knee joint with a gait cycle of 1 s. As shown in Figure 22, the maximum required damping force is 293 N. Therefore, to satisfy the damping requirement under this gait condition, the maximum damping force of the MR damper should exceed 293 N. The experimental results in Section 4 show that the maximum damping force of the MR damper reaches 367 N, which is higher than the design requirement. This indicates that the semi-active mode of the LMRA is feasible.

6. Control method of the SCMRPK

Both the driving and damping regulation of the SCMRPK are realized by the LMRA. The LMRA can output active driving force and controllable damping force, allowing the SCMRPK to operate in both active and semi-active modes. This section introduces the control methods for these two modes, and the block diagram of the control system is shown in Figure 23. The SCMRPK control system mainly consists of a controller, a controlled current source, position sensors, a force sensor, a motor driver, and the LMRA.

https://doi.org/10.1017/S0263574726103610 Published online by Cambridge University Press

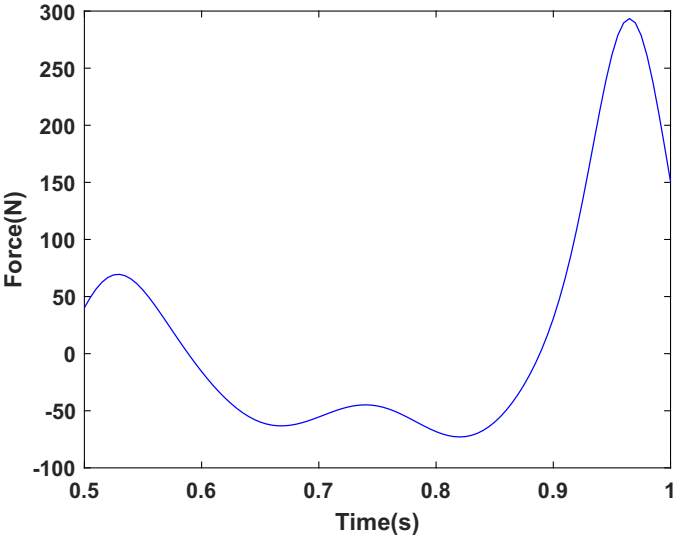


Figure 22. *Time history of the required damping force of the MR damper of the prosthetic knee joint during the swing phase with a gait cycle of 1 s.*

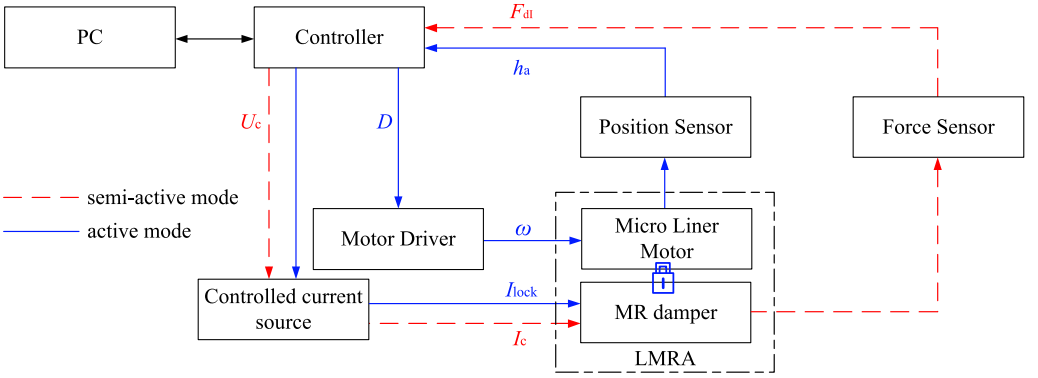


Figure 23. *Block diagram of the control system for the SCMRPK.*

6.1 Semi-active control method

The red dashed loop in Figure 23 represents the semi-active mode control loop. In the semi-active mode, the SCMRPK adopts the computed torque and PD feedback control algorithm to achieve trajectory tracking, which is realized by regulating the damping force of the MR damper to control the prosthetic knee joint angle θ_{4d}.

According to Eqs. (13), (14), (16), and (18), the controlled damping force (F_{dC}) generated by the MR damper is given by

$$\begin{aligned} F_{dC} &= T_{2C}\frac{\delta\theta_{2d}}{\delta d} = T_{2C}\frac{\partial\theta_{2d}}{\partial\Delta d} \\ &= \left[M_{21}\ddot{\theta}_1 + M_{22}\left(\ddot{\theta}_{d2} + K_{D1}\dot{e}_f + K_{P1}e_f\right) + M_{23}\ddot{\theta}_3 + M_{24}\ddot{\theta}_4 + C_2 + G_2\right]\frac{\partial\theta_{2d}}{\partial\Delta d} \end{aligned} \tag{20}$$

where T_{2C} is the controlled torque around the axis K_2; θ_{d2}, which is calculated using both Eq. (18) and the reference knee angle, is the reference knee angle of θ_2; e_f ($=\theta_{d2}$–θ_2) is the tracking error; K_{P1} is the proportionality factor, and K_{D1} is the derivative time constant.

https://doi.org/10.1017/S0263574726103610 Published online by Cambridge University Press

Considering that the MR damper can only provide the passive damping force, the MR damper is unable to provide the necessary active force when the F_{dC} is positive during the swing's flexion phase or negative during the swing's extension phase. The damping force (F_{dI}) provided by the MR damper can be determined by

$$\begin{aligned} &if\ \dot{\theta}_{2d} \le 0 \\ &F_{dI} = \begin{cases} F_{dmax} & F_{dC} < -F_{dmax} \\ F_{dmin} & F_{dC} > -F_{dmin} \\ -F_{dC} & otherwise \end{cases} \\ &if\ \dot{\theta}_{2d} > 0 \\ &F_{dI} = \begin{cases} F_{dmax} & F_{dC} > F_{dmax} \\ F_{dmin} & F_{dC} < F_{dmin} \\ F_{dC} & otherwise \end{cases} \end{aligned} \tag{21}$$

where F_{dmax} is the maximum damping force generated by the MR damper and F_{dmin} is the damping force generated by the MR damper with the current of 0 A.

According to Eqs. (20) and (21), the required F_{dI} provided by the MR damper can be achieved by adjusting the current in the excitation coil (I_c).

To accurately determine the controlled current of the MR damper, its current-driving equation was established based on the experimental data in Section 4, as follows:

$$I_c = c_3 F_{dM}^3 + c_2 F_{dM}^2 + c_1 F_{dM} + c_0 \tag{22}$$

where $c_3 = 2.246 \times 10^{-7}$, $c_2 = 1.22 \times 10^{-5}$, $c_1 = 2.269 \times 10^{-2}$, and $c_0 = -0.5731$; F_{dM} is the measured damping force of the MR damper.

The relationship between the controlled current in the coils (I_c) output from the controlled current source and the input control voltage (U_c) can be expressed as follows:

$$U_c = k_I I_c \tag{23}$$

where k_I is the proportionality factor of the controlled current source.

According to Eqs. (20), (22), and (23), the F_{dI} of the LMRA can be generated by adjusting the input voltage (U_c), thereby controlling the flexion angle (θ_{4d}) of the prosthetic knee joint.

6.2 Active control method

In the active mode, the prosthetic knee joint is actively driven by controlling the micro linear motor to drive the telescopic pole. The blue loop in Figure 23 represents the active mode control loop. The controller applies a locking current I_{lock} to the coils so that the damper outputs a large damping force and the system can be regarded as approximately rigidly connected. When the load force is smaller than the damping force, the relative displacement between the piston tube and the outer cylinder can be neglected.

For the micro linear motor, PD control is adopted to output the PWM duty cycle (D) so as to regulate the motor speed and thereby control the displacement of the telescopic pole. According to Eqs. (16)–(19), the displacement of the telescopic pole can be converted into the angle θ_{2d} of the second link relative to the vertical direction, thereby realizing the control of the knee flexion angle θ_{4d}. The control process can be expressed as follows:

$$\begin{cases} e_\theta = \theta_{d2d} - \theta_{2d} \\ D = k_1 e_\theta \\ \omega = K_{D2}\dot{D} + K_{P2} D \end{cases} \tag{24}$$

https://doi.org/10.1017/S0263574726103610 Published online by Cambridge University Press

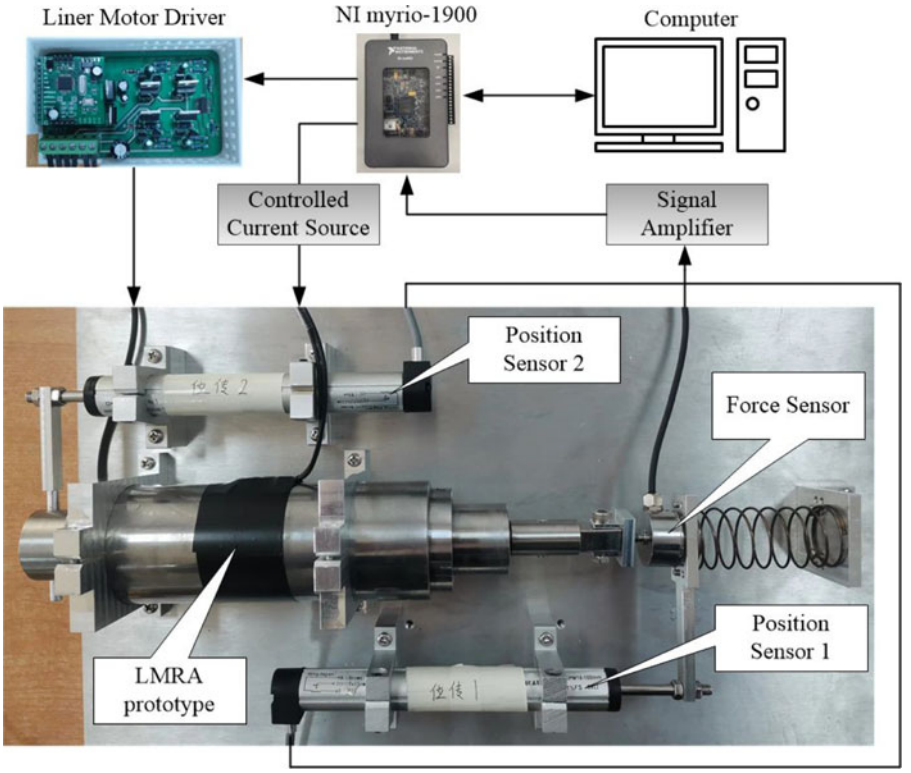


Figure 24. *The experimental setup of LMRA in active mode.*

where θ_{d2d} is the reference angle of θ_{2d} calculated according to Eqs. (17), (18) and the reference angle of the knee joint; e_θ ($=\theta_{d2d}-\theta_{2d}$) is the tracking error; k_1 is the proportionality factor between the duty cycle and the tracking error; K_{P2} is the proportionality factor, and K_{D2} is the derivative time constant.

According to the above control method, in the semi-active mode, the motor does not operate and the damping force is regulated by the current I_c; in the active mode, the motor operates and the damper is controlled by the locking current I_{lock}. Switching between the two modes is realized through motor start-stop control and switching of the control current (I_c and I_{lock}).

7. Testing of LMRA in active mode

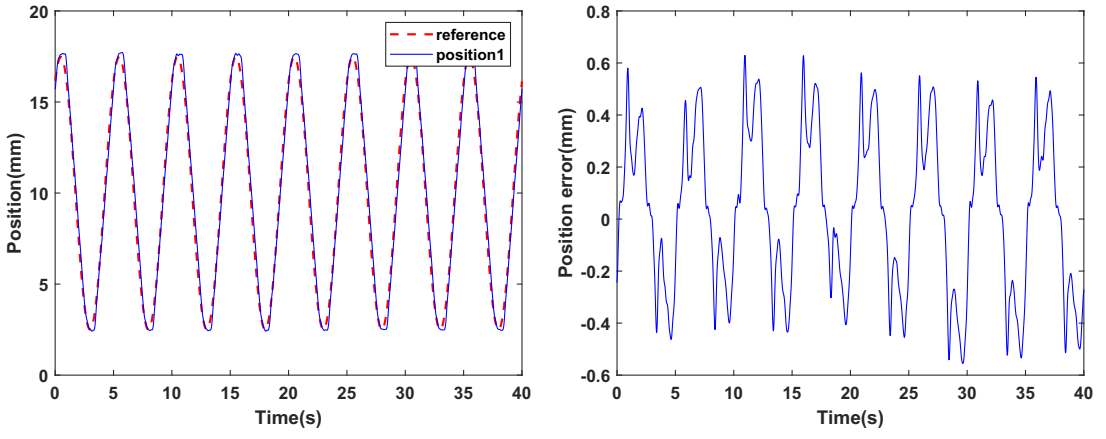
7.1. Experiment setup

To verify the performance of the LMRA in active mode, the experimental setup shown in Figure 24 was established. The setup mainly consists of the LMRA prototype, a controller (type: NI myRIO-1900, National Instruments), a micro linear motor (type: BTL-20, maximum speed: 20 mm/s, maximum force: 150 N, Changzhou Louie Linear Actuator Company), a motor driver, two position sensors (type: MIRAN KPM18, Shenzhen MIRAN Company), a force sensor (type: DYMH-103, Bengbu Dayang Company), and a signal amplifier (type: DY510-4, Bengbu Dayang Company).

As shown in Figure 24, the LMRA prototype and the two position sensors are fixed to the experimental platform. The force sensor is mounted between the motor's telescopic pole and the spring to measure the output force of the LMRA, while the spring is used to simulate the load.

The sensing end of position sensor 1 is fixed to the force sensor and is used to measure the position of the motor's telescopic pole, whereas the sensing end of position sensor 2 is fixed to the piston rod and is used to measure the displacement of the outer cylinder of the damper relative to the micro linear motor.

https://doi.org/10.1017/S0263574726103610 Published online by Cambridge University Press



(a) (b)

Figure 25. *Displacement tracking and tracking error curves of the motor telescopic pole: (a) displacement tracking curve; (b) tracking error curve.*

The controller regulates the controlled current source to supply the locking current I_{lock} to the coil. The sensor signals are amplified by the signal amplifier before being sent to the controller. Based on these signals, the controller outputs control signals to the motor driver, thereby controlling the motion of the motor telescopic pole.

7.2. Experiment results and analysis

As long as the damping force generated by the locking current exceeds the load force, the corresponding current can be regarded as the locking current under that load. To evaluate the performance of the LMRA in active mode, an experiment was conducted with a locking current of 1.5 A applied to the MR damper. In the experiment, the motor telescopic pole was controlled to track a sinusoidal displacement signal with a frequency of 0.2 Hz and an amplitude of 7.5 mm. The displacement tracking curve of the motor telescopic pole and the corresponding tracking error curve are shown in Figure 25(a) and (b), respectively. According to Figure 25(b), the maximum position error between the actual position and the reference position is about 0.628 mm, and the maximum relative position error is 8.37%. The delay between the actual position and the reference position is about 0.095 s. Since human reaction time is typically between 0.15 s and 0.40 s ref. [46], the measured delay is acceptable for daily prosthesis use.

To verify the effect of the locking current, an experiment was conducted under a locking current of 1.5 A. Figure 26 shows the time history of the force acting on the telescopic pole during its motion under this condition. Figure 27 shows the time history of the relative displacement between the outer cylinder of the damper and the micro linear motor during the motion of the telescopic pole under the same condition. As shown in Figure 26, the force signal measured by the force sensor starts to increase after 4 s, reaches a maximum value of 75 *n* within 1 s, and then remains approximately constant. Figure 27 shows that the maximum displacement between the outer cylinder and the micro linear motor is 0.044 mm. These results indicate that effective locking is achieved and that the active mode of the LMRA is feasible.

8. Testing of SCMRPK

Figure 28(a) and (b) show the block diagram and photographs of the SCMRPK experimental setup, respectively. The setup consists of a controller (type: YXSPACE-SP6000, Nanjing Yanxun Company), a controlled current source (type: OPA549, Chengdu Yike Company), a sensor unit, a motor driver, and

https://doi.org/10.1017/S0263574726103610 Published online by Cambridge University Press

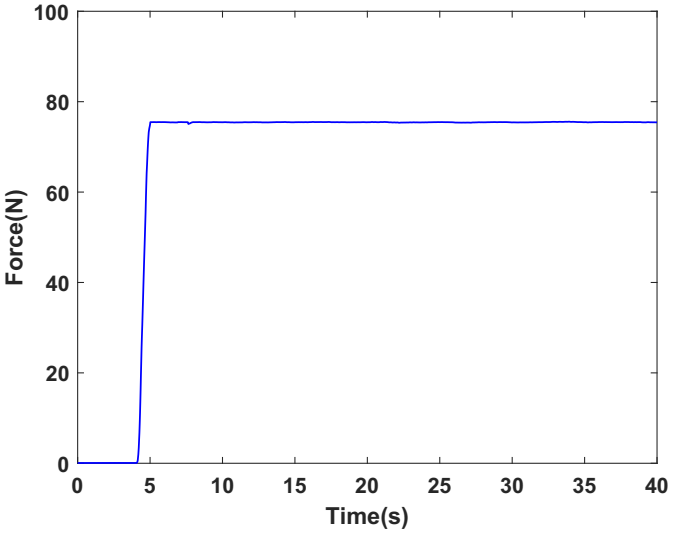


Figure 26. *Time history of the force acting on the telescopic pole during its motion under 1.5 A current.*

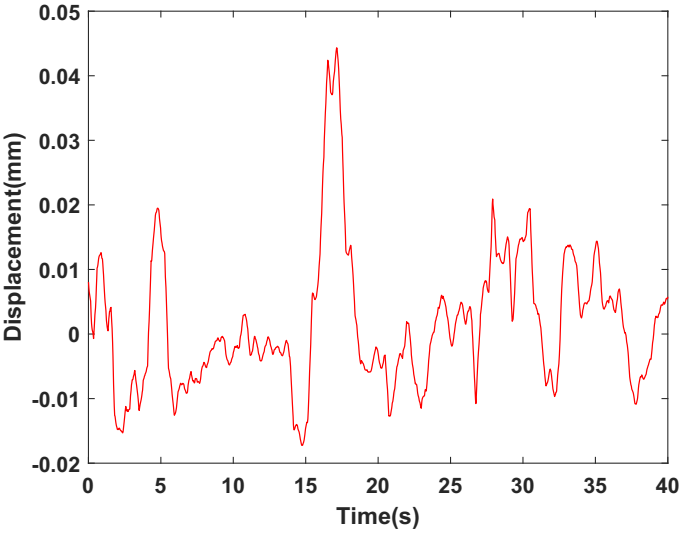


Figure 27. *Time history of the relative displacement between the outer cylinder of the damper and the micro linear motor under 1.5 A current.*

the SCMRPK prototype. The sensor unit includes one micro position sensor and two angle sensors. A micro position sensor (type: PM11-2, linearity: 0.015 mm, Taizhou Quantum Electronic Technology Company) is embedded in the prosthetic shank to measure the relative displacement (Δd) of the piston rod for monitoring the locking status of the LMRA in active mode. Angle sensor AS1 (type: WDD35S2, linearity: 0.1 mm, Shanghai Huiren Company) is coaxially mounted on the hip joint synchronization mechanism (HJSM) to measure the swing angle (θ_1) of the TSM. Angle sensor AS2 (type: GTC, accuracy: 0.022°, Taizhou Quantum Electronic Technology Company) is coaxially mounted on the K_2 axis to measure the angle (θ_{2d}) between the second link and the vertical direction.

https://doi.org/10.1017/S0263574726103610 Published online by Cambridge University Press

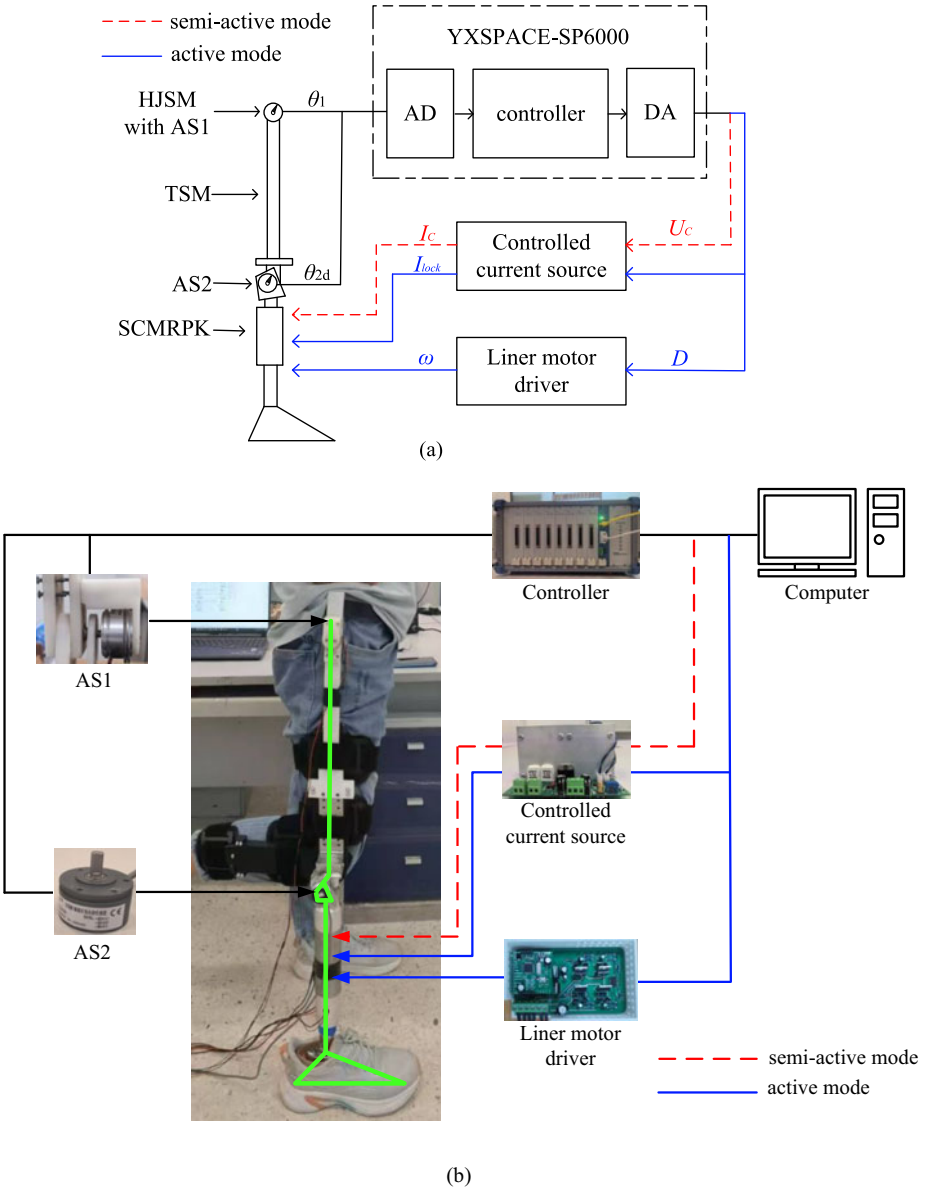


Figure 28. *(a) the block diagram and (b) the photograph of the SCMRPK experimental setup.*

8.1 Semi-active mode experiment

The semi-active mode experiment was conducted using the setup shown in Figure 28. In this mode, the sensor unit transmits the acquired signals to the controller, and the controller governs the SCMRPK according to Eqs. (13), (14), (16), (18), and (20)–(22). The controlled current source then converts the control voltage (U_c) generated by the controller into the coil current (I_c), as indicated by the red line in Figure 28.

In the experiment, the SCMRPK-based lower limb prosthesis was attached to the subject's hip through a connector, and its motion was driven by the subject's thigh swing. Figure 29(a) and (b) show the time histories of the knee joint angle ($-\theta_{4d}$) under the proposed control algorithm at walking speeds of 0.8 m/s and 1.2 m/s, respectively, in comparison with the reference angle θ_{d4d} (0° to 56°). The results show that,

https://doi.org/10.1017/S0263574726103610 Published online by Cambridge University Press

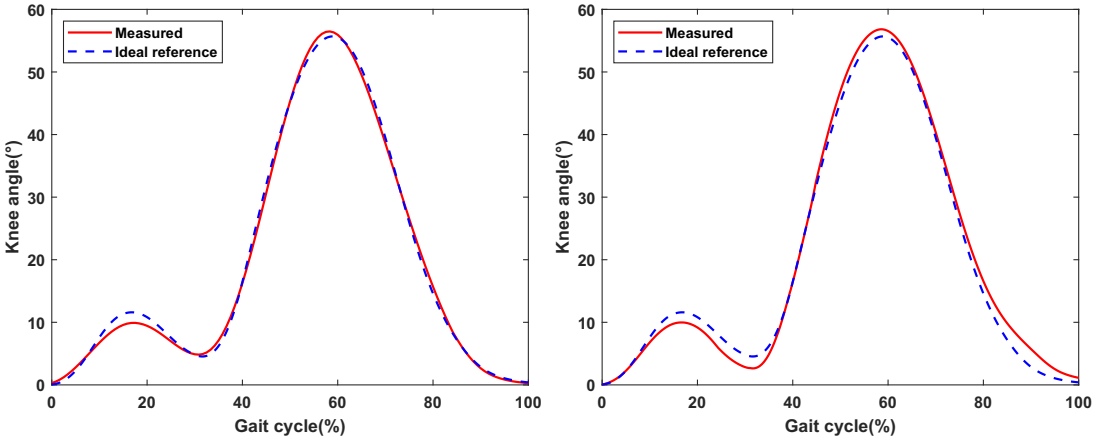


Figure 29. *Time histories of the measured knee angle ($-\theta_{4d}$) of the SCMRPK with the controlled current by the algorithm developed in this paper for (a) 0.8 m/s, (b) 1.2 m/s walking speeds and the ideal reference knee angle.*

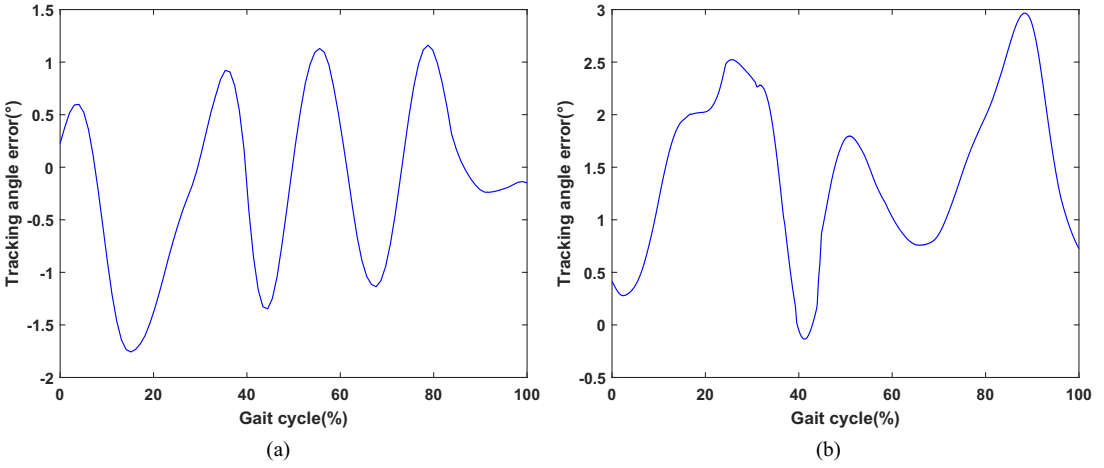


Figure 30. *Time histories of the tracking angle error between the measured knee angle ($-\theta_{4d}$) of the SCMRPK with the controlled current by the algorithm developed in this paper for (a) 0.8 m/s and (b) 1.2 m/s walking speed and the ideal reference knee angle.*

at walking speeds of 0.8 m/s and 1.2 m/s, the knee joint angle ranges from 0.25° to 56.47° and from 0.04° to 56.83°, respectively, which are in good agreement with the reference angle.

In addition, the time history of the tracking angle error between the measured knee angle ($-\theta_{4d}$) and the ideal reference knee angle under the control current is shown in Figure 30. Observing Figure 30(a) and (b), at a walking speed of 0.8 m/s, the maximum absolute tracking angle error is 1.76°, the maximum relative tracking angle error is 3.14%, and the root mean square (RMS) error is 0.51°; at a walking speed of 1.2 m/s, the maximum absolute tracking angle error is 2.97°, the maximum relative tracking angle error is 5.31%, and the RMS error is 1.54°.

The experimental results show that the proposed control method can effectively reduce the tracking angle error. During the stance phase, stability is mainly ensured by the mechanical characteristics of the four-bar linkage and the user's self-regulation. Rapid error correction during the swing phase is

https://doi.org/10.1017/S0263574726103610 Published online by Cambridge University Press

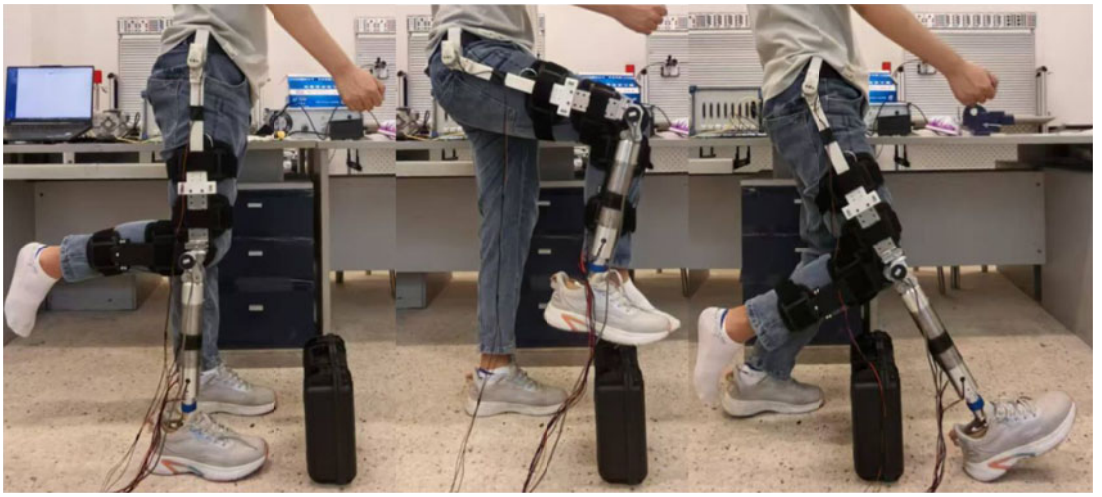


Figure 31. *The motion process of the lower limb prosthesis while crossing an obstacle under active control.*

beneficial to motion coordination. Overall, the SCMRPK can accurately track the reference knee joint angle throughout the entire gait cycle.

8.2 Active mode experiment

The experimental setup is shown in Figure 28. Compared with the semi-active mode, the active mode additionally involves motor-driver control. The sensor unit transmits the acquired signals to the controller. According to the control method established in Section 6.2, θ_{2d} is regulated to control the knee joint angle θ_{4d}.

During obstacle-crossing experiments, the controller instructs the SCMRPK to generate a large knee flexion angle to assist the test subject in crossing the obstacle. Figure 31 shows the motion process of the lower limb prosthesis crossing a 0.3 m obstacle under active control. Figure 32 shows the time history of the measured knee angle ($-\theta_{4d}$) of the SCMRPK under the current controlled by the algorithm developed in this paper during the obstacle-crossing process. The obstacle-crossing process can be divided into three stages. First, a locking current is applied so that the damper forms an approximately rigid connection. Then, the motor drives the knee joint to flex to about 80°. Finally, after the obstacle is crossed, the motor drives the knee joint to extend, thereby completing the obstacle-crossing motion.

In summary, the semi-active mode of the SCMRPK can be achieved by controlling the damping force of the MR damper. When the load force is smaller than the damping force, the active mode of the SCMRPK can adjust the flexion angle by adjusting the displacement of the motor telescopic pole. The test results show that the proposed SCMRPK can operate effectively in both semi-active and active modes.

9. Conclusion

This paper presents a systematic study on the structural design, magnetic circuit design, dynamic modeling, control methods, and experimental validation of the SCMRPK. The main conclusions are as follows:

1. A structurally compact magnetorheological prosthetic knee joint with obstacle-crossing function, namely the SCMRPK, was designed. The SCMRPK is formed by combining a four-bar linkage

https://doi.org/10.1017/S0263574726103610 Published online by Cambridge University Press

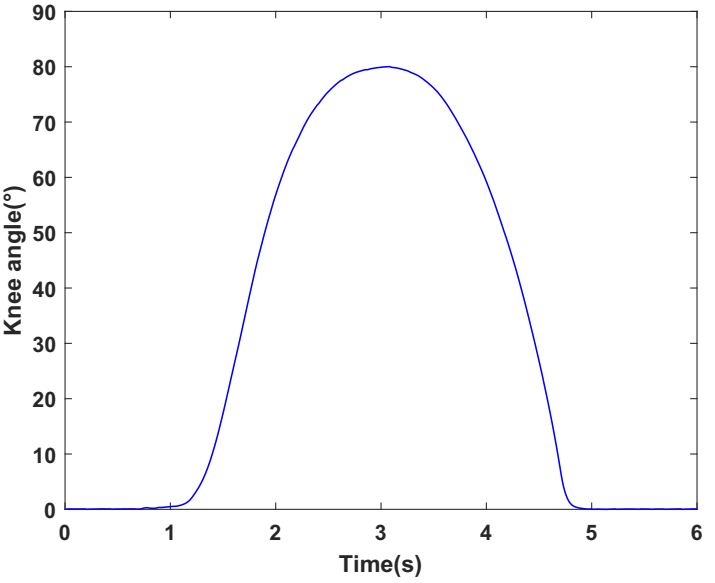


Figure 32. *Time history of the measured knee angle ($-\theta_{4d}$) of the SCMRPK under the current controlled by the algorithm developed in this paper during the obstacle-crossing process.*

mechanism and a LMRA. By integrating a micro linear motor into the piston rod of an MR damper, the LMRA combines the active mode and the semi-active mode, enabling it to output driving force in the active mode and controllable damping force in the semi-active mode. Under dimensional constraints, the SCMRPK combines bionic rotational characteristics, semi-active damping regulation capability, and active driving capability.

2. A key dimensional design method for the LMRA magnetic circuit was proposed. Simulation analysis and experimental testing were carried out on the magnetic circuit of the LMRA with the integrated micro linear motor, and the results verified the effectiveness of the designed magnetic circuit.
3. The kinematic and dynamic models of the SCMRPK-based lower limb prosthesis were established, and the control methods for the semi-active mode and the active mode were designed.
4. A displacement tracking test was carried out for the LMRA in active mode. The results show that, under a locking current of 1.5 A, the telescopic pole can achieve stable displacement tracking, which verifies the feasibility of the active mode of the LMRA.
5. Semi-active gait experiments and active obstacle-crossing experiments of the SCMRPK were completed. The semi-active experimental results show that, at a walking speed of 1.2 m/s, the root mean square error between the measured knee angle of the SCMRPK and the ideal knee angle is 1.54°. The active experimental results show that the SCMRPK-based lower limb prosthesis can cross an obstacle with a height of about 0.3 m.

In summary, the proposed SCMRPK is not only compact in structure but also enables a relatively natural gait and obstacle crossing.

Author contributions. Lei Xu was responsible for the research conception and system design. Lei Xu and Chao Wang contributed to the manuscript writing and revision. Qiuxia Fan and Qianqian Zhang were responsible for the research methodology and project supervision. Lei Xu, Chao Wang, and Yuhui Liu participated in the experimental validation, data processing, and analysis.

Financial support. This research was funded in part by the Fundamental Research Program of Shanxi Province (No. 202403021211212), the Postdoctoral Fellowship Program and China Postdoctoral Science Foundation (No. 2025M774384),

https://doi.org/10.1017/S0263574726103610 Published online by Cambridge University Press

the Key Country Science and Technology Cooperation Project under the Shanxi Provincial Science and Technology Cooperation and Exchange Special Program (Grant No. 202304041101007), and the National Key Research and Development Program of China—Sub-project on Integration Technology of Laser Interferometry System and Inertial Sensors (Grant No. 2024YFC2207100).

Competing interests. The authors declare no conflicts of interest.

Ethical approval. Not applicable.

Use of AI. AI tools were not used in the research or writing of this paper.

References

[1] M. S. H. Bhuiyan, I. A. Choudhury and M. Dahari, "Development of a control system for artificially rehabilitated limbs: A review," *Biol. Cybern*. **109**(2), 141–162 (2015).
[2] M. J. Highsmith, J. T. Kahle, R. M. Miro, M. S. Orendurff, A. L. Lewandowski, J. J. Orriola, B. Sutton and J. P. Ertl, "Prosthetic interventions for people with transtibial amputation: Systematic review and meta-analysis of high-quality prospective literature and systematic reviews," *J. Rehabil. Res. Dev*. **53**(2), 157–184 (2016).
[3] R. M. A. Dutra, R. M. de Andrade, A. B. Soares, N. V. Thakor and C. B. S. Vimieiro, "Magnetorheological fluid in prostheses: A state-of-the-art review," *J. Intel. Mat. Syst. Str*. **35**(5), 485–516 (2024).
[4] X. Zhou, G. Liu, B. Han, H. Li, L. Zhang and X. Liu, "Different prevention and treatment strategies for Knee Osteoarthritis (KOA) with various lower limb exoskeletons–A comprehensive review," *Robotica* **39**(8), 1345–1367 (2021).
[5] M. U. Qadir, I. U. Haq, M. A. Khan, K. Shah, H. Chouikhi and M. A. Ismail, "Design, analysis, and development of low-cost state-of-the-art magnetorheological-based microprocessor prosthetic knee," *Ah S. Sens*. **24**(1), 255 (2024).
[6] S. Negi, U. Sagar, V. K. Nautiyal and N. Sharma, "Design and analysis of magnetorheological damper based ankle–foot prosthesis prototype," *Ind. Robot*. **49**(2), 240–248 (2022).
[7] S. Kumar, S. Chandramohan and S. Sujatha, "Geometric optimization of magnetorheological damper for prosthetic ankles using artificial neural networks," *Mechatronics* **98**, 103108 (2024).
[8] S. Kumar, S. Chandramohan and S. Sujatha, "Optimal design of magnetorheological valve using the coupling of FE magnetic analysis and MOGA optimization for prosthetic ankle," *J. Vib. Eng. Technol*. **12**(2), 2205–2217 (2024).
[9] S. Kumar, M. S. Reddy and S. Chandramohan, "Shape optimization of parametric curve-based magnetorheological damper valve for augmented performance in prosthetic ankle applications," *Smart Mater. Struct*. **34**(7), 075041 (2025).
[10] S. Kumar, M. S. Reddy and S. Chandramohan, "Shape optimization of MR damper valve for prosthetic ankles using magnetic FEM-GA approach with gait simulation integration," *Results Eng*. **27**, 106315 (2025).
[11] C. Khazoom, C. Veronneau, J.-P. L. Bigue, J. Grenier, A. Girard and J.-S. Plante, "Design and control of a multifunctional ankle exoskeleton powered by magnetorheological actuators to assist walking, jumping, and landing," *IEEE Robot. Autom. Lett*. **4**(3), 3083–3090 (2019).
[12] Q. Shi, Y. Lin, K. Nie, X. Zhao, X. Bai, X. Wu, W.-H. Liao and F. Gao, "Design and testing of magnetorheological brake with adjustable interdigitated combs for lower limb prostheses and exoskeletons," *Smart Mater. Struct*. **34**(5), 055031 (2025).
[13] T. Kikuchi, K. Oda, S. Yamaguchi and J. Furusho, "Leg-robot with MR clutch to realize virtual spastic movements," *J. Intel. Mat. Syst. Str*. **21**(15), 1523–1529 (2010).
[14] J. Xu, Y. Li, L. Xu, C. Peng, S. Chen, J. Liu, C. Xu, G. Cheng, H. Xu, Y. Liu and J. Chen, "A multi-mode rehabilitation robot with magnetorheological actuators based on human motion intention estimation," *IEEE T. Neur. Sys. Reh*. **27**(10), 2216–2228 (2019).
[15] J. D. Carlson, W. Matthis and J. R. Toscano, "Smart Prosthetics Based on Magnetorheological Fluids," **In:** *Smart Structures and Materials 2001: Industrial and Commercial Applications of Smart Structures Technologies* (A. M. R. McGowan ed.), Vol. 4332 (SPIE, Newport Beach, CA, United States, 2001) pp. 308–316.
[16] J. H. Kim and J. H. Oh, "Development of An Above Knee Prosthesis Using MR Damper and leg Simulator," **In:** *Proceedings 2001 ICRA IEEE International Conference on Robotics and Automation*, Vol. 4, (ICRA, Seoul, Korea, 2001) pp. 3686–3691.
[17] H. Herr and A. Wilkenfeld, "User-adaptive control of a magnetorheological prosthetic knee," *Ind. Robot*. **30**(1), 42–55 (2003).
[18] H. M. Herr, A. Wilkenfeld and O. Bleck, "Speed-adaptive and patient-adaptive prosthetic knee: U.S," Patent 6,610,101[P]. (2003).
[19] Q. Zuo, J. Zhao, X. Mei, F. Yi and G. Hu, "Design and trajectory tracking control of a magnetorheological prosthetic knee joint," *Appl. Sci*. **11**(18), 8305 (2021).
[20] Q. Fu, D.-H. Wang, L. Xu and G. Yuan, "A magnetorheological damper-based prosthetic knee (MRPK) and sliding mode tracking control method for an MRPK-based lower limb prosthesis," *Smart Mater. Struct*. **26**(4), 045030 (2017).
[21] H. Song, Y. Cao, W. Chen, L. Ren, Y. Ma, K. Wang, X. Wang, Y. Zhang and L. Ren, "Design, testing and control of a magnetorheological damper for knee prostheses," *J. Bionic. Eng*. **21**(4), 1788–1800 (2024).
[22] R. S. T. Saini, H. Kumar and S. Chandramohan, "Optimal design of flow mode semi-active prosthetic knee dampers," *Sci. Iran. Trans. B Mech. Eng*. **29**(6), 3049–3062 (2022).

https://doi.org/10.1017/S0263574726103610 Published online by Cambridge University Press

[23] Z. Song, W. Zhang, D. Chen, W. Ju, R. Kang and J. S. Dai, "A bianisotropic damper based on magnetorheological fluid for a quasi-passive load-bearing exoskeleton," *IEEE/ASME Trans. Mechatronics* **30**(3), 2316–2326 (2024).
[24] W. Wang, X. Liang, L. Li, L. Gong, L. Deng, X. Hu, S. Zhang and S. Sun, "Wearable chairless exoskeleton capable of flexible support to relieve muscle fatigue for industrial workers," *Smart Mater. Struct*. **33**(12), 125041 (2024).
[25] X. P. Do, B. Q. L. Mai, B. H. Kang and S. B. Choi, "Design of a New Magneto-Rheological Damper Featuring a Hybrid Type of Piston for Lower Limb Exoskeleton," *Sensors and Smart Structures Technologies for Civil, Mechanical, and Aerospace Systems 2019*, Vol. 10970, SPIE (2019) pp. 790–794.
[26] J. B. Morrison, "The mechanics of the knee joint in relation to normal walking," *J. Biomech*. **3**(1), 51–61 (1970).
[27] S. A. Gard, D. S. Childress and J. E. Uellendahl, "The influence of four-bar linkage knees on prosthetic swing-phase floor clearance," *J. Prosthet. Orthot*. **8**(2), 34–40 (1996).
[28] J. W. Bneakey and S. H. Marquette, "Beyond the four-bar knee," *J. Prosthet. Orthot*. **10**(3), 77–80 (1998).
[29] C. Ochoa-Diaz, T. S. Rocha, L. de Levy Oliveira, M. E. G. Paredes, R. S. Lima, A. P. L. Bó and G. A. Borges, "An Above-Knee Prosthesis with Magnetorheological Variable-Damping," **In:** *5th IEEE RAS/EMBS International Conference on Biomedical Robotics and Biomechatronics* (IEEE, São Paulo, Brazil, 2014) pp. 108–113.
[30] H. L. Xie, Z. B. Liu, J. Y. Yang, "Modelling of magnetorheological damper for intelligent bionic leg and simulation of knee joint movement control," *Int. J. Simul. Model*. **15**(1), 144–156 (2016).
[31] L. Xu, D.-H. Wang, Q. Fu, G. Yuan and L.-Z. Hu, "A novel four-bar linkage prosthetic knee based on magnetorheological effect: Principle, structure, simulation and control," *Smart Mater. Struct*. **25**(11), 115007 (2016).
[32] N. Mohamed, A. I. Alateyah and W. H. El-Garaihy, "Defect free optimization of a polycentric prosthetic knee design using imperialist competition-inspired optimization method," *J. Eng. Res-KUWAIT*. **11**(2B), 337–349 (2023).
[33] J. Zhang, G. Hu, J. Zhao and W. Zhu, "Trajectory tracking control of a four-bar linkage prosthetic knee with magnetorheological damper," *J. Magn. Magn. Mater*. **610**, 172537 (2024).
[34] G. Liu, F. Gao, D. Wang and W.-H. Liao, "Medical applications of magnetorheological fluid: A systematic review," *Smart Mater. Struct*. **31**(4), 043002 (2022).
[35] J. Park, G.-H. Yoon, J.-W. Kang and S.-B. Choi, "Design and control of a prosthetic leg for above-knee amputees operated in semi-active and active modes," *Smart Mater. Struct*. **25**(8), 085009 (2016).
[36] R. M. Andrade, A. B. Filho, C. B. S. Vimieiro and M. Pinotti, "Optimal design and torque control of an active magnetorheological prosthetic knee," *Smart Mater. Struct*. **27**(10), 105031 (2018).
[37] O. Arteaga, H. C. Terán, H. V. Morales, E. M. Argüello, M. I. Erazo, M. Ortiz and J. J. Morales, "Design of human knee smart prosthesis with active torque control," *Int. J. Mech. Eng. Robot. Res*. **9**(3), 347–352 (2020).
[38] F. Gao, Y. N. Liu and W. H. Liao, "Design of Smart Prosthetic Knee Utilizing Magnetorheological Damper," **In:** *Sensors and Smart Structures Technologies for Civil, Mechanical, and Aerospace Systems 2017* (J. P. Lynch ed.), Vol. 10168 (SPIE, Portland, Oregon, United States, 2017) pp. 373–380.
[39] F. Gao, Y. N. Liu and W. H. Liao, "Optimal design of a magnetorheological damper used in smart prosthetic knees," *Smart Mater. Struct*. **26**(3), 035034 (2017).
[40] H. Ma, B. Chen, L. Qin and W.-H. Liao, "Design and testing of a regenerative magnetorheological actuator for assistive knee braces," *Smart Mater. Struct*. **26**(3), 035013 (2017).
[41] B. Chen, X. Zhao, H. Ma, L. Qin and W.-H. Liao, "Design and characterization of a magneto-rheological series elastic actuator for a lower extremity exoskeleton," *Smart Mater. Struct* **26**(10), 105008 (2017).
[42] W. Wang, L. Deng, G. Yun, W. Li, L. Yu, S. Zhu, J. Yang, W. Li, S. Zhang, X. Gong and S. Sun, "Design and validation of a body-powered lower extremity exoskeleton featuring explosive locomotion augmentation," *IEEE/ASME Trans. Mechatronics.* **31**(3), 2633–2644 (2026).
[43] B. F. Spencer Jr., S. J. Dyke, M. K. Sain and J. D. Carlson, "Phenomenological model of a magnetorheological damper," *J. Eng. Mech. ASCE* **123**(3), 230–238 (1997).
[44] D. L. Grimes, W. C. Flowers and M. Donath, "Feasibility of an active control scheme for above knee prostheses," *J. Biomech. Eng*. **99**(4), 215–221 (1977).
[45] D. L. Grimes, *An Active Multi-mode Above Knee Prosthesis Controller* (Massachusetts Institute of Technology, 1979).
[46] J. Z. Chen and W. H. Liao, "Design, testing and control of a magnetorheological actuator for assistive knee braces," *Smart Mater. Struct*. **19**(3), 035029 (2010).

Cite this article: L. Xu, C. Wang, Q. Fan, Q. Zhang and Y. Liu (2026). "Development of a structurally compact magnetorheological prosthetic knee joint with obstacle-crossing function", Robotica **44**, 2284–2312. https://doi.org/10.1017/S0263574726103610

https://doi.org/10.1017/S0263574726103610 Published online by Cambridge University Press